UNIVERSITY OF HELSINKI REPORT SERIES IN PHYSICS

HU-P-D225

Molecular dynamics simulation of elastic and sputtering properties of nanowires

Andrey Ilinov

Division of Materials Physics
Department of Physics
Faculty of Science
University of Helsinki
Helsinki, Finland

ACADEMIC DISSERTATION

To be presented with the permission of the Faculty of Science of University of Helsinki,
for public criticism in auditorium B123 of Exactum (Kumpulan kampus),
on February 27th 2015, at 12 o'clock noon.

HELSINKI 2015

ISBN 978-952-10-8979-4 (printed version)
ISSN 0356-0961
Tampere 2015
Juvenes Print

ISBN 978-952-10-8980-0 (PDF version)
http://ethesis.helsinki.fi
Helsinki 2015
Electronic Publications @ University of Helsinki (Helsingin yliopiston verkkojulkaisut)

Andrey Ilinov, **Molecular dynamics simulation of elastic and sputtering properties of nanowires**, University of Helsinki, 2015, 52 p. + appendices, University of Helsinki Report Series in Physics, HU-P-D225, ISSN 0356-0961, ISBN 978-952-10-8979-4 (printed version), ISBN 978-952-10-8980-0 (PDF version)

ABSTRACT

Nanotechnology became an emerging field during the last few decades. The possibility to create elements having sizes in the nanometer range provides new opportunities for medical applications, various sensors and detectors, and composite materials technologies. However, at the nanoscale the basic physical properties may change unexpectedly including chemical, mechanical, optical and electronic properties. There is still no clear understanding of all possible consequences of miniaturization on the behavior of nanostructures.

This thesis is focused on the analysis of mechanical and structural (including sputtering under irradiation) properties of nanorods. By nanorods we imply structures like beams or rods, with their cross-sectional diameter measuring in nanometers and having a length several times larger than the diameter. At such sizes it becomes possible to simulate the structures atom by atom using the molecular dynamics (MD) method.

In the first part of the thesis, we analyze the elastic properties of Si nanorods: how the variation in size may change the elastic moduli, the effects of oxidation and intrinsic stresses. We also check the validity of the classical continuum mechanics approach by modeling the same nanorods with the finite elements method (FEM).

In the second part we investigate sputtering from Au nanorods under ion irradiation. Recent experiments had shown that there is a big enhancement of sputtering yields from Au nanorods in contrast with those from a flat surface. The yields can be as much as 1000 per individual impact. MD gives us an opportunity to analyze the sputtering process with a femtosecond resolution which is impossible by any of the existing experimental methods. We find that an explosive ejection of nanoclusters is the main factor causing such large sputtering yields.

Contents

ABSTRACT iii

1 INTRODUCTION 1

2 PURPOSE AND STRUCTURE 3
2.1 Summaries of the original publications 3
2.2 Author's contribution 5

3 METHODS 6
3.1 Molecular Dynamics simulations 6
3.2 Simulation of ion radiation effects by MD 8

4 Elastic properties of Si nanorods 13
4.1 Nanowires elastic tests 13
4.2 Si-O potentials comparison for bulk systems 15
4.3 Simulation setup 19
4.4 Creation of the oxide layer 20
4.5 Analysis of stress 22
4.6 Tensile tests 22
4.7 Three point bending tests 24
4.8 Finite Element Modeling of the three point bending tests 26
4.9 Results 28

5 Xe irradiation of Au nanorods 32
5.1 Irradiation experiment 32
5.2 Simulation setup 34
5.3 Results 35

6 Discussion and Conclusions 40

ACKNOWLEDGEMENTS 43

REFERENCES 44

1 INTRODUCTION

Nanotechnology became an emerging field of research only recently, when atomic level analysis methods became widely available, mainly after the invention of a scanning tunneling microscopy in 1981 [1]. Surprisingly, people had already worked with nanosystems for centuries; for example, the color of glass used in mosaics depends on the sizes of embedded metal nanoparticles [2]. Generally, nanotechnology is a manipulation of objects which have at least one of their dimensions in the nanometer range: individual atoms, molecules, nanoclusters, fullerenes, nanowires, carbon nanotubes, thin films. Currently, industrial applications are mostly limited to the passive use of bulk nanomaterials [3]: silver nanoparticles prevent the growth of bacteria [4], zinc oxide nanoparticles are used in sun protective cosmetics [5], and so on. Further miniaturization is especially important for development of micro- and nano-electromechanical devices, because it generally provides - along with the size reduction - a shorter time response, higher performance, enhanced sensitivity and decreased energy consumption. Such devices are used as e.g. miniaturized sensors and detectors, parts of optoelectronic equipment, or logical circuits [6, 7]. Other promising applications of nanosystems include further development of durable and light weight composite materials, nanomedicine, membranes and filters, catalyzers, and many others [8–12].

One should have in mind, that at the nanoscale the surface to volume ratio becomes high, which affects most of the material properties, including electronic, magnetic, optical, chemical and mechanical ones [13–17]. The importance of mechanical properties is crucial because every designed device must be in the first place mechanically reliable. In this work, we study the mechanical properties of nanowires and nanorods. The difference between them is that nanowires have lengths at least 10 times bigger than their diameters, whereas nanorods can be shorter. The mechanical properties of nanorods are more difficult to analyze; for instance, when testing the elastic behavior by bending, shear stresses in short nanorods become dominant [18], whereas in long nanowires they can simply be neglected.[1] Unfortunately, there is still no clear understanding of how the mechanical properties of nanowires and nanorods differ from those of macroscopic systems. Depending on the material and the analysis techniques, nanowires had been found stiffer [19] or softer [20] than a bulk material, and also having similar variations in the yield strength [21, 22].

In the first part of the thesis we investigate the elastic properties of Si nanorods. Si nanorods and nanowires can be relatively easily integrated with already existing equipment used for production of electronic circuits. Therefore, they are very promising as details of nano-electromechanical systems. The large piezoresistance effect of Si nanorods [23] makes them suitable for use in mechanical or chemical sensing devices as a sensitive part; they provide a possibility to produce miniaturized and highly sensitive accelerometers [24]. Other potential applications include nanoresonators and field-emission devices [13, 25].

---

[1] Further in the text these terms may be used as synonyms, and the length-to-diameter ratio effects are described explicitly.

For such applications, it is crucial to understand the elastic behavior of Si nanorods, along with their electronic properties. There is a number of publications where the mechanical properties of Si nanowires [26–28] have been investigated. Those works are mostly focused on differences from the properties of bulk Si and size-related effects. However, the influence of oxidation has not been studied deeply yet. Here we perform simple stretching and three point bending studies for Si nanorods of different sizes with diameters ranging from 6 to 16 nm and having different oxidation levels by means of MD, in order to estimate the elastic moduli and compare them with the values obtained by using a classic continuum mechanics approach. Nanowires of such sizes have not been thoroughly tested experimentally yet, as they are difficult to produce using existing methods. MD gives us an opportunity to 'construct' such nanowires atom-by-atom and also to introduce an oxide coating in a controllable manner. To verify the applicability of the continuum mechanics approximations we have modeled the same systems by the finite element method. This gives an opportunity to take into consideration anisotropy of a Si core, intrinsic stresses, as well as the small length to diameter ratio of the tested nanorods.

In the second part of the thesis, we simulate irradiation of gold nanowires by 80 keV Xe ions in order to estimate sputtering yields. Gold is a good electricity conductor and also highly corrosion resistant. For this reason, gold nanorods are perfectly suitable for biosensing and medical applications [29], as well as for catalyst applications. Recent experiments have revealed a huge enhancement of sputtering yields from gold nanorods in contrast to an ordinary flat gold surface [Publication **I**]; the yields were up to 1000 sputtered atoms per individual impact. It was unclear what mechanism causes such large yields, and there are no experimental methods yet that have good enough time resolution to analyze the evolution of collision cascades. The MD method nowadays is capable of simulating nanorods of realistic sizes, providing the possibility to investigate the sputtering process with a femtosecond resolution and to track the trajectories of individual atoms. In our simulations an explosive ejection of nanoclusters is observed during the thermal spike events, leading to craters formation and fast nanorods degradation. These effects should be taken into account when radiation processing of metal nanorods is performed.

2 PURPOSE AND STRUCTURE

The main purpose of this thesis is to provide a better understanding of the nanosize-related effects on the mechanical and structural properties of nanorods, including elastic behavior of Si nanorods and the sputtering properties of gold nanorods. The MD method has been used, as it gives a possibility to model easily bending tests on Si nanorods of realistic sizes with a different thickness of an oxide coating. On the other hand, the time resolution of MD makes it possible to analyze the evolution of collision cascades and track the motion of individual atoms when irradiating gold nanorods.

This thesis is based on four publications; they are referred to by bold-face Roman numerals. The structure of the thesis is as follows. In the following section, the four publications are summarized and the author's contribution is explained. Section 3 contains a general overview of the computational methods used in this thesis: the classical MD method, and the special additions to the basic MD algorithm needed to simulate high energy particles collisions are described. Section 4 contains details about the Si nanorods characterization techniques, comparison of Si-O potentials, description of the simulation setup, how the oxide layer was formed, the analysis of stresses and the obtained elastic moduli. Comparison of the MD results with the results obtained by FEM is also presented in this section. The experiment of irradiating gold nanorods by Xe ions, as well as the corresponding sputtering simulations are presented in Section 5. Finally, in section 6 the major results of this thesis are summarized and discussed.

2.1 Summaries of the original publications

Publication I: Enhanced sputtering yields from single-ion impacts on gold nanorods

G. Greaves, J.A. Hinks, P. Busby, N.J. Mellors, A. Ilinov, A. Kuronen, K. Nordlund, S.E. Donnelly, *Physical Review Letters* **111(6)**, 065504 (2013)

This work describes the first experimental observation of large sputtering yields caused by 80 keV Xe ion irradiation of monocrystalline gold nanorods. The obtained yields were in the range of 100-1900 atoms per ion, which is more than an order of magnitude larger than the typical values observed in similar conditions from a flat gold surface. This enhancement was partly caused by the proximity of collision cascades and resulting thermal spikes to the nanorod surfaces. To get a better understanding of the sputtering processes at the atomic level, we have simulated a similar experimental setup by the means of molecular dynamics. The analysis of the simulation results has revealed that the largest number of atoms was explosively ejected in a form of atomic clusters, which made the major contribution to the enhanced yield.

Publication II: Atomistic modeling of bending properties of oxidized silicon nanowires

A. Ilinov, A. Kuronen, *Journal of Applied Physics* **115**, 104305 (2014)

In this work, we model a simple stretching and a three point bending tests of monocrystalline Si nanowires using molecular dynamics simulations, in order to investigate their elastic properties. Tested nanowires were about 30 nm in length and had diameters from 5 to 9 nm. To study the influence of a native oxide, nanowires were covered with a 1 nm thick silica layer. The bending force was applied by a carbon hemisphere with a 5 nm diameter. We have evaluated the elastic properties of various Si-O potentials and found that the Tersoff Si-O parameterization by Munetoh [31] gives the most accurate description for various Si systems. In order to remove the indentation effect of the diamond hemisphere and to obtain a pure bending behavior, we have also performed a set of simulations where the bottoms of the nanowires were fixed. Our simulations demonstrate that the oxide layer reduces the nanowire stiffness when compared with a pure Si nanowire with the same number of silicon atoms, in spite of the fact that the oxidized nanowires had larger diameters.

Publication III: Sputtering yields exceeding 1000 by 80 keV Xe irradiation of Au nanorods

A. Ilinov, A. Kuronen, K. Nordlund, G. Greaves, S.E. Donnelly, *Nuclear Instruments and Methods in Physics Research B* **341**, 17-21 (2014)

This manuscript extends the analysis of 80 keV Xe ion impacts on monocrystalline gold nanorods performed in Publication **I**. Using MD simulations, we show that the highest yields can be understood as a combination of enhancements due to low incoming angles at the sides of the nanorod, as well as the high surface-to-volume ratio causing explosive sputtering from heat spikes. We also find, both in experiments and simulations, that channeling has a strong effect on the sputtering yield: if the incoming beam happens to be aligned with a crystal axis of the nanorod, the yield can decrease to less than 100 atoms per impact, because it becomes probable the ion goes through without depositing any significant amount of energy to Au atoms.

Publication IV: Size-dependent elastic properties of oxidized silicon nanorods

A. Ilinov, A. Kuronen, *Journal of Applied Physics* **116**, 204305 (2014)

This work extends the study started in Publication **II**. Here we simulate a three point bending test for Si nanorods of different sizes with an oxide coating of different thickness using molecular dynamics simulations and the finite element modeling (FEM). We tested nanorods with diameters from 6 to 16 nm which had lengths from 31 to 62 nm. Our aim was to estimate how well the elastic properties of Si nanorods can be described using the classical continuum mechanics approach, and to evaluate the size related effects. The agreement between MD simulations and FEM calculations was consistent for the pristine Si nanorods of all sizes, whereas the oxidized Si nanorods with small length-to-diameter ratio had much smaller effective bending moduli than predicted by FEM. Our assumption is that it is due to the significant decrease of the shear modulus in the oxide layer of the smallest nanorods. We have also introduced surface stresses into the FEM models and found that their influence on bending properties is more important for partially oxidized nanorods.

2.2 Author's contribution

The author carried out the MD simulations for publications **I** and **III** and performed the analysis of the results of those simulations. For publication **I** the author wrote the part of the manuscripts describing the simulation methods, and for publication **III** the author wrote the majority of the manuscript except the parts describing the experimental techniques.

The author carried out all the simulations in publications **II**, **III**, **IV**, and also performed the majority of analysis of the results. Writing of these manuscripts was mainly carried out by the author.

3 METHODS

3.1 Molecular Dynamics simulations

Molecular dynamics (MD) is a way to simulate the evolution of atomic positions in time by incrementally solving the Newton's equations of motion. This method was firstly suggested in 1957 by Alder and Wainwright [32, 33]. In material science, individual atoms and their interactions are usually modeled. However, with some modifications, the same approach can be applied for simulating even planets and galaxies [34]. Of course, it could not be achieved without coarse-graining, so planets or stars play role of 'atoms' in such calculations.

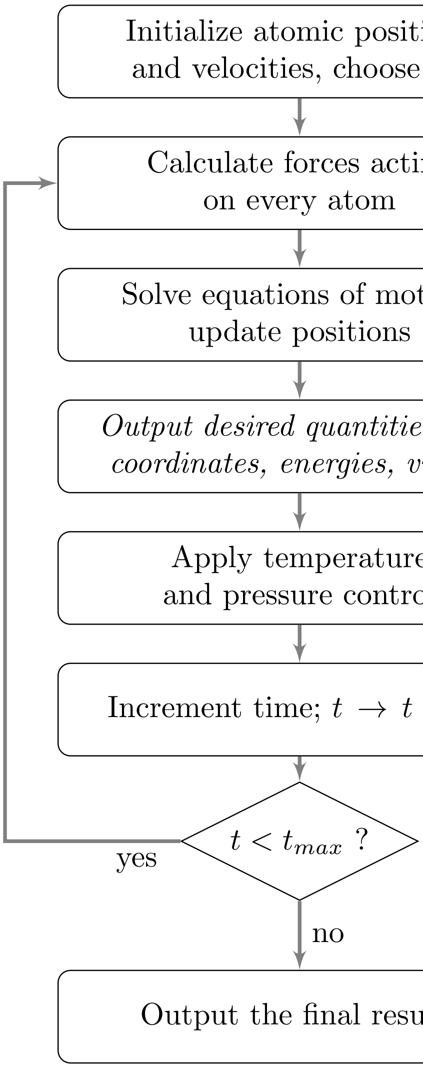

Figure 1: Basics steps of the MD algorithm.

A simplified algorithm of the MD method is presented on Fig. 1. Classical MD is based on the Born-Oppenheimer approximation. The assumption is that electrons move much faster than atomic nuclei, and any electronic excitation reaches its equilibrium state instantly compared to timescales relevant to atomic motion, and regardless of the motion of atoms. Hence, electronic subsystem is not explicitly taken into account in classical MD and always assumed to be in the ground state.

Let's take a closer look at the algorithm. At the beginning, for every atom $i = 1 \ldots N$ in a system of N atoms we should set initial positions $\mathbf{r}_i$ and may also assign initial velocities $\mathbf{v}_i$ generated according to the Maxwell distribution, which corresponds to the initial temperature of the system. In addition, we should define an expression for the potential energy $V(\mathbf{r}^N)$ between atoms, called the 'interatomic potential'. It is usually based on ab-initio (first principle) calculations or fitted to experimental data. After that, the atomic trajectories of the atoms are calculated iteratively; the forces acting on each atom are determined according to the selected potential $V(\mathbf{r}^N)$

$$\mathbf{F}_i = -\nabla_{\mathbf{r}_i} V(\mathbf{r}^N), \text{ where } \mathbf{r}^N = (\mathbf{r}_1, \mathbf{r}_2, \ldots \mathbf{r}_N) \tag{1}$$

Then, Newton's equation of motion

$$m_i \mathbf{a}_i = m_i \frac{\partial^2 \mathbf{r}_i}{\partial t^2} = \mathbf{F}_i \tag{2}$$

are integrated over a small time step Δt using a numerical integration algorithm, such as velocity Verlet [35] or Gear5 [36]. Here m_i and $\mathbf{a}_i$ denote the mass and the acceleration of atom i.

It is important to select an appropriate timestep Δt used in integration. The timestep should depend on the maximum velocity of atoms in a specific system: if Δt is too long, the system will behave unphysically, the total energy will not be conserved and the system may 'explode'. When Δt is too short, the computational time will be wasted for nothing, giving results of the same precision as with the optimal timestep. In case of a system where the kinetic energies of atoms do not change significantly, a constant timestep based on the maximum expected velocity that atoms may achieve is usually used. In pure MD simulations, in most cases Δt cannot be more than ≈ 10 fs for any real material, which practically limits the total modeled time to microseconds.

The MD algorithm described above is used in case of a micro-canonical ensemble, where the number of atoms, the volume of the simulation cell, and the total energy is preserved. To alter the energy of the system, e.g. to heat up an object to obtain an anneal effect, or to remove an excessive energy introduced after an ion impact, the algorithm can be complemented with a temperature control.

The simple and efficient thermostating method was suggested by Berendsen et al. [37]. The system temperature T is controlled by coupling to an external heat bath with desired constant temperature T_0. Since the temperature of the system is determined by velocities of the atoms, the temperature control can be achieved by scaling the velocities every timestep by factor λ:

$$\lambda = \sqrt{1 + \frac{\Delta t}{\tau_{\mathrm{T}}} (\frac{T_0}{T} - 1)} \tag{3}$$

where τ_{T} is the time constant determining the scaling rate. The value of τ_{T} parameter should be chosen carefully, so that it is small enough to adjust the system temperature with a sufficient rate. However, τ_{T} should not be too low, to still allow for natural fluctuations of atomic velocities. The method can be applied either to the entire system, or just at the borders of the simulation cell. In contrast to other thermostating methods [38–40], the Berendsen thermostat does not preserve a canonical ensemble suppressing realistic (physical) temperature fluctuations, nevertheless it appears reasonably accurate and effectively converges to the desired temperature T_0.

A similar scaling technique can be applied to control a pressure P in the system at the desired level P_0 by changing the system size and scaling the atomic coordinates in all three X, Y, Z dimensions simultaneously, or only along the selected directions. The scaling factor μ is defined as:

$$\mu = \sqrt[3]{1 - \frac{\beta \Delta t}{\tau_{\mathrm{P}}}(P_0 - P)} \tag{4}$$

where $\beta = 1/E_{\mathrm{bulk}}$ is the isothermal compressibility of the system, used solely to make the time constant τ_{P} independent on the simulated material. This method has also been suggested by Berendsen [37] and is therefore called the Berendsen pressure control.

MD method is computationally heavy and even on a modern hardware, system sizes are generally limited to hundreds of millions of atoms. If it is needed to simulate a bulk system with an infinite lattice, such a situation can be approximated by using periodic boundary conditions. This means that when an atom moves through a border of the simulation cell, it reappears from the opposite side, and all interactions are also 'wrapped' around edges. However, it should be taken into consideration that when the bounding box size is too small, unphysical self-interactions become an issue; e.g. defects may start to interact with themselves through strain fields in the cell [41].

The MD code used for this study is mainly PARCAS [42, 43].

3.2 Simulation of ion radiation effects by MD

MD method provides a number of features that make it suitable for studying ion irradiation effects in solids. Before we discuss these, however, it is necessary to outline the physical processes that occur when a high energy ion hits an object. Due to interactions with an electronic subsystem and atomic nuclei, the ion loses kinetic energy, a process called ion stopping. Complete definition of the stopping power S states, that it is an average slowing down force acting on charged particles in matter, which leads to decrease of the particle's energy. S is generally a function of energy specific for every material and ion combination, and numerically equal to the energy loss per unit path length: $S(E) = -dE/dx$. Ion stopping is caused by various reasons, and they are detailed in what follows.

Electronic stopping is a process of slowing down of an incoming ion due to inelastic collisions with bound electrons in the medium. The number of collisions with electrons that the ion may undergo is very large, and the ion charge state changes frequently while moving through the medium. Therefore, the precise account of all possible interactions with electrons would be very difficult to achieve. Moreover, in the classical MD algorithm, the electronic subsystem is not taken into consideration directly, so the electronic stopping power is usually approximated as a simple function of energy $S_e(E)$ [44, 45] which works as a 'frictional force' slowing down the ion.

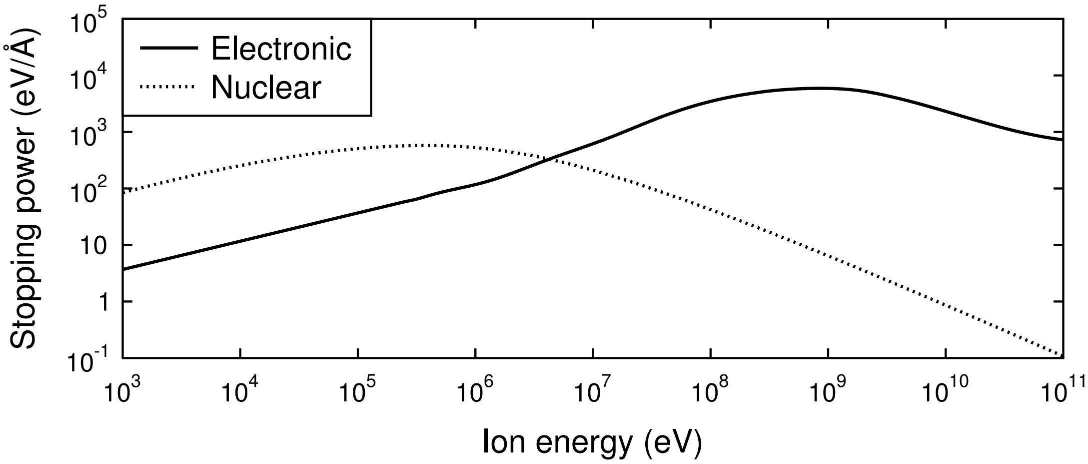

Figure 2: Electronic and nuclear stopping for Xe ions in Au, calculated by SRIM [46].

The second important mechanism, nuclear stopping, defines slowing down due to elastic collisions between the ion and atomic nuclei composing the matter, which can be simulated directly in MD. Fig. 2 demonstrates the contribution of electronic and nuclear stopping powers for Xe ions in gold for different ion energies, calculated by SRIM [46]. The maximum of the nuclear stopping power corresponds to the energy $\approx$ 500 keV per ion for this combination of elements, and for the electronic stopping - near 1 GeV.

If the repulsive potential $V(r)$ between interacting atoms is specified, it becomes possible to calculate the nuclear stopping power $S_n(E)$. Electronic stopping starts to dominate over nuclear stopping at energies bigger than $\approx$ 5 MeV, as illustrated in Fig. 2. Nuclear stopping prevails for ions having a heavy mass, while for light ions penetrating heavy materials, the nuclear stopping is weaker than the electronic stopping in the entire energy range [47].

If the incoming ion has a large initial energy in the MeV range, then at the beginning it is slowed mainly by the electronic stopping, and it moves almost along a straight path. When the ion energy decreases sufficiently, collisions with nuclei become more and more probable, finally dominating the stopping process. When atoms of the solid receive significant recoil energies after being hit by the ion, they can escape from their lattice sites producing a cascade of further collisions in the material. Such collision cascades are the main cause of a damage production during ion implantation in metals and semiconductors. Once energies of all primary and secondary recoils in the system decrease below the certain minimal energy, necessary to displace an atom from its site in the lattice (the threshold displacement energy), the production of any extra damage stops.

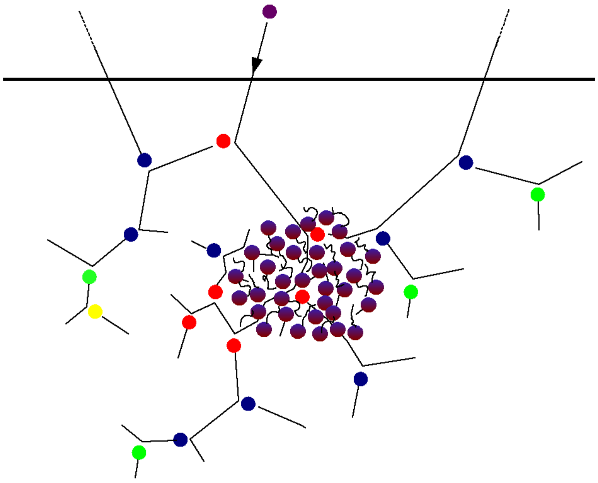

Figure 3: Collision cascade scheme. The thick horizontal line corresponds to the surface, the purple circle is the incoming ion. Red, blue, green and yellow circles illustrate primary, secondary, tertiary and quaternary recoils, respectively. The dense purple region in the center demonstrates a heat spike event involving multiple neighboring atoms [48].

If the incoming particle is a heavy ion having energy in keV or MeV range, and the material is dense enough, there is a possibility that collisions appear very close to each other, becoming a complicated process of many-body interactions that involves thousands of neighboring atoms, which is called a heat spike. In this region the ions move in complex paths, while at the beginning during the ballistic phase the trajectories are almost linear between individual collisions, as shown on Fig. 3.

The kinetic energies of atoms involved in a heat spike are usually around 1 eV, which corresponds to a 'temperature' of the order of 10000 K. It has been demonstrated that after several lattice vibrations, the kinetic energy distribution of the atoms in a heat spike becomes the Maxwell-Boltzmann distribution [49]. However, heat spikes cool down to the ambient temperature in 1 to 100 ps, so the 'temperature' here cannot be treated as a thermodynamic equilibrium temperature.

The MD method makes it possible to model many-body interactions that occur during the thermal spike events, and analyze the ion irradiation effects at the atomic level with a sufficient degree of accuracy. The ballistic phase of the cascade, when the incoming ion and its lower-order recoils have energies much bigger than the threshold displacement energy, typically lasts less than 1 ps; at this stage a very small timestep Δt is needed for energy conservation. If a heat spike is formed, it may last up to around 100 ps, until the spike temperature has cooled down essentially to the ambient temperature [50], so it may be necessary to apply one of the temperature control algorithms in MD simulations to remove the excessive energy, as would happen in a real experiment. The relaxation stage of the cascade, when the formed defects have a possibility to recombine and migrate, can last from a few ps up to infinite times, depending on the material properties and the ambient temperature. As the duration of MD simulations is usually limited to nanoseconds, it is common to supplement the MD with some other methods, like Kinetic Monte-Carlo, to analyze the defect migration and recombination [51].

At energies between 0.01 and 10.0 MeV, both the electronic and the nuclear stopping mechanisms are usually important, so the total stopping power can be expressed as a sum of the two terms: $S(E) = S_e(E) + S_n(E)$. Even at projectile energies of tens of eV the part of a total energy is still dissipated due to electronic stopping, and this has to be taken into account in MD simulations [52]. The electronic energy loss is generally introduced in MD simulations as a frictional force acting on rapidly moving atoms. Several semi-empirical models giving stopping power as a function of the ion kinetic energy have been developed [45, 53]. It had been demonstrated that the model given by Ziegler, Biersack and Littmark [45] (the so called 'ZBL' stopping) gives an acceptable accuracy in ion range calculations [54, 55]. The ZBL model implemented in the SRIM code [56] has been used for estimating the electronic stopping power for Xe ions in Au, which in turn was used in our MD simulations.

For even higher energies in the GeV range, it may be necessary to consider the radiative stopping due to the emission of bremsstrahlung (electromagnetic radiation), produced during deceleration of a charged particle when deflected by an atomic nucleus [57]. The moving particle loses its kinetic energy, which is converted into a photon. Such effect is mostly important for high energy electron irradiation and therefore outside the scope of this thesis.

In high energy collisions, the distance between atoms may become shorter than would ever be possible under equilibrium conditions. Most interatomic potentials are fitted to equilibrium properties, such as elastic constants, the lattice constant, the cohesive energy; but they may give a poor description or can even be undefined at very short ranges. Since the interatomic potential determines the scattering behavior during elastic collisions and therefore the nuclear stopping, it is crucial for cascade simulations that the potential is also accurate at short distances. To achieve this, it is common to complement the ordinary equilibrium potential with a more accurate repulsive short range potential at distances that are shorter than the equilibrium atomic separation [58].

As the reason for repulsion at short distances r is the Coulomb interaction between atomic nuclei, high energy repulsive potentials usually have the form

$$V(r) = \frac{Z_1 Z_2 e^2}{4\pi\epsilon_0 r}\Phi(r/a) \tag{5}$$

where $\Phi(x)$ is a screening function and $a = a(Z_1, Z_2)$ stays for a screening length; Z_1 and Z_2 are the atomic numbers. The screening function represents the fact that at normal interatomic distances the electron shells screen the nuclei. The nuclei almost don't see each other, and consequently $\Phi \approx 0$ and the low-energy interactions dominate. When the distance between nuclei is short enough, the electron clouds unite and the screening effect mostly disappears. The interaction is then almost purely Coulombic, and $\Phi \approx 1$.

The short range potential can be obtained from ab-initio calculations [59]. In majority of cases it is reasonable to use the ZBL universal repulsive potential [45], which typically gives inaccuracies of approximately $5 - 10\%$ for a chosen elements combination.

As have been explained in Section 3.1, the timestep Δt should be selected according to the maximal velocity that a particles may have. In simulations of ion irradiation, at the beginning of the run (ballistic stage) the incoming ion and its recoils have very high velocities and Δt needs to be very short so the atomic trajectories remain correct and the energy is conserved. As the particles cool down or sputter far away from the system, it may be beneficial to decrease Δt for computational efficiency. Therefore, at such non-equilibrium simulations it is usually reasonable to utilize a variable timestep, short at the beginning and increasing as the atoms come to rest. The following adaptive time step selector is used in PARCAS [60]:

$$\Delta t = \min\left(a\frac{k_t}{v_{\max}}, \frac{E_t}{Fv_{\max}}, 1.1\Delta t, \Delta t_{\max}\right), \tag{6}$$

where k_t and E_t are proportionality constants, $v_{\max}$ is the maximum velocity of any atom in the system, and $\Delta t_{\max}$ is the maximum permitted timestep, ensuring a reasonable integration even if the atomic velocities approach zero. Using this scheme, Δt is allowed to change not more than 10% each simulation step to prevent sudden changes. In strong collisions, the velocity can drop instantly, although the acceleration is high, hence the time step is made dependent on the maximum force F. Additionally, if a particle flies far away from the system, it is usually considered as sputtered and for computational efficiency not taken into account for timestep evaluation, even having a high velocity.

4 Elastic properties of Si nanorods

4.1 Nanowires elastic tests

Mechanical characterization of one-dimensional nanostructures like nanowires with acceptable accuracy remains a challenging task for experimental science. For instance, reported measured Young's moduli values for Si nanowires vary from 0.3 to 1.5 of the bulk material value [61]. The discrepancies are significant even for samples having the same characteristic size, and there is no consensus on size-related effects. The possible sources of inaccuracies are most likely related to the calibration of equipment for applying loads and measuring displacements, fixing and mounting of samples, determination of nanowire diameter or cross-sectional area, and correct estimation of applied boundary conditions [7].

The nanowires characterization methods are based either on the direct loading, or on vibrational properties. The most common techniques are presented in Fig. 4.

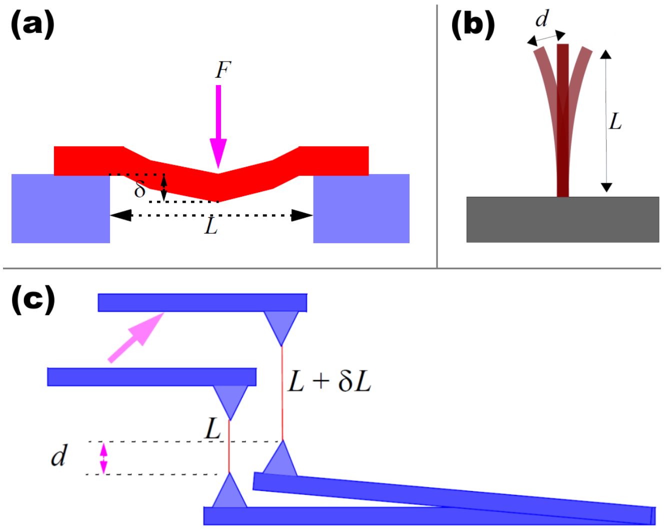

Figure 4: Experimental techniques for measuring the elastic properties of nanowires: a) AFM bending test; b) dynamic resonance; c) AFM tension test. Dr. Antti Kuronen is acknowledged for providing the pictures.

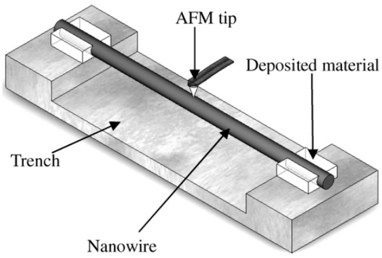

Figure 5: Sketch of a common three point bending experimental setup at the nanoscale [62].

A large group of tests utilizes the Atomic Force Microscopy (AFM) unprecedented force and displacement resolutions. The three point flexural test, demonstrated in Figs. 4a and 5, is a widely used experimental method to evaluate the elastic properties of beams. It can also be implemented at the nanoscale: a nanowire is bridged over a trench and ends of the nanowire are rigidly mounted to the substrate by either an electron beam induced deposition or by a polymer adhesive [63]. Subsequently, a bending force is applied to the middle point by a tip of an AFM microscope. Analyzing the force-deflection curve, one can estimate the bending modulus of the nanowire (the relevant equations are described in Section 4.7). The experimental setup can be modified by depositing the nanowire on a flat and hard substrate instead of the trench, making it possible to perform nanoindentation measurements for e.g. evaluating the hardness. The bending test can also be applied for a free standing nanowire fixed only from one end to the substrate (similar to those that are presented on Fig. 4b). Such a setup is called a simple (two-point) bending; it has slightly different boundary conditions, but the overall principles remain the same as in case of the three point bending.

To avoid strain gradients and high stress concentration below an AFM tip during bending experiments, the tensile test experimental setup has been suggested by Yu et al. [64]. The nanowire is connected between two AFM probes; the lower one is a relatively soft load sensor, and the upper one is a stiffer actuator attached to a piezo-based linear motor (Fig. 4c). The system is then installed inside the SEM chamber, which is used to measure the deflection of the soft AFM cantilever. The force-deflection response is evaluated from the stiffness calibration of the AFM probes. Such a setup can be used to measure the Young's modulus; if the nanowire is pulled with big enough force, plastic deformations will occur and the nanowire will eventually break, giving the value of the failure strength.

The second important group of methods is based on the fact, that when only one end of the nanowire is fixed, it is easy to excite vibrations in it by e.g. applying an alternating electric field. When the field frequency becomes equal to one of the natural nanowire frequencies (corresponding to a certain vibration mode), the vibrational amplitude increases significantly due to the resonance effect. It can be observed as blurring of a TEM image, because the time needed for capturing the image is much larger than the vibration period. According to Euler-Bernoulli beam model, the frequencies of vibration are

$$\nu_i = \frac{a_i^2}{2\pi}\sqrt{\frac{EI}{\rho A L^4}} \tag{7}$$

where ρ is a material density, E denotes the Young's modulus, I is the second area moment, a_i defines a coefficient specific for each vibration mode, L is the nanowire length with cross-sectional area A. According to the latter equation, a Si nanowire with a diameter 10 nm and length 200 nm should have the frequency of the first vibration mode at the order of $\approx$ 350 MHz. The resonance based technique provides a direct visualization of the effect, and manipulations on the nanowire are usually significantly simplified as the nanowire is already attached to the substrate during the Vapour-Liquid-Solid (VLS) growth. However, the surface elasticity effects may affect the results more than in other characterization methods due to the gradient dominated type of deformation [19].

In spite of the fact that all methods are essentially based on the same elastic properties, in real experiments different loading methods often yield different values of the Young's moduli for similar nanowires [7, 61]. The differences are expected to emerge in the tension and bending (resonance) tests in case of significant surface effects, as the surface of the nanowire carries a bigger fraction of stress during the flexural motion [65].

To correctly interpret the bending results, one should consider that for short beams (nanorods) having a small length-to-diameter ratio, the total deflection becomes a superposition of deformations due to bending and shear. For an isotropic beam with a cylindrical cross section, the ratio of the shear (δ_{shear}) and bending (δ_{bend}) contributions can be estimated from the relationship [18, 66]:

$$\frac{\delta_{\text{shear}}}{\delta_{\text{bend}}} = \frac{20}{3}(1+\nu)\left(\frac{D}{L}\right)^2 \tag{8}$$

where ν is the Poisson's ratio and D/L is the diameter to length ratio of the bent nanorod. For silica $\nu = 0.19$ [67], and it can be estimated that if $L/D \geq 20$, the contribution of shear is less than 2% and the measured effective bending modulus becomes approximately equal to the Young's modulus value [66].

In this work, we have simulated nanorods of different sizes and with different L/D ratios, the 5.8×31 nm, 7.9×46 nm and 10.4×62 nm nanorods have $L/D \approx 5.7$ in the pristine and $L/D_{ox} \approx 3.6$ in the fully oxidized states, whereas the 5.8×63 nm nanorod has $L/D = 10.8$ and $L/D_{ox} = 6.7$ respectively. So, $\delta_{\text{shear}}/\delta_{\text{bend}}$ is estimated to be up to 0.65 for the fully oxidized nanorods from the first group, and 0.16 for the 5.8×63 nm fully oxidized nanorod.

4.2 Si-O potentials comparison for bulk systems

Silicon is widely regarded as an important material for the modern technology, and there is variety of interatomic potentials that have been developed to model and predict its properties. However, if we are interested in structures that can also contain SiO_2, Si suboxides and their interfaces - we are mostly limited to several variations of the Tersoff-based many body interatomic potentials [31, 68], the Silica-Watanabe [69], and the Keating-type potentials [70, 71]. The ReaxFF force field has also been parameterized for simulating Si and O systems [72], but due to its complexity, it is computationally expensive and still prohibitive for modeling nanowires of realistic size that contain hundreds of thousands of atoms. For this study the Tersoff-based potential optimized for Si-O systems by Munetoh et al. [31], and the Samela-Watanabe potential [73, 74], a modification of the original Silica Watanabe potential [69] improved for better energy conservation, were selected for testing, as both of the potentials were fitted taking into account various properties of multiple Si-O compounds.

Si is a semiconductor and has a lattice of the diamond type, i.e. every atom in the lattice is surrounded by exactly four neighbors. The bonds are predominantly of the covalent type, and the position of nearest neighbors is such that if one atom is in the middle of a regular tetrahedron, its four neighbors are at the corner sites of this tetrahedron. Hence, the angle between any two bonds of the same atom becomes $\theta_0 = \arccos(-1/3) \approx 109.5°$. Because of the nature of the electron orbitals hybridization, the covalent bonds typically have a strong directional dependence, and some angles between the bonds are preferred over the others. For instance, the energy of three covalently bonded atoms depends not only on the distances, but also on the angles between them. This property is often used for construction of the interatomic potentials; it is possible to introduce an angular term in the functional form which gives a minimum of the potential energy at the equilibrium angle θ_0.

The Silica-Watanabe potential is essentially based on the Stillinger-Weber formalism [75] and parameterized for Si-O systems. This is a three-body potential of the 'explicit-angular' type, i.e. there is a term in the functional form containing the θ_0 which reduces the potential energy when the angle between atoms approaches θ_0. The original potential gives a reasonable description of various properties of Si, including the elastic characteristics [69]. However, it is important to realize that the angle between bonds is always 'forced' to the ideal tetrahedral angle θ_0 with the angular term, which is not physically motivated and unrealistic. Hence, the potentials of this type always give a minimum at only the specified angle, which may limit the predictive capabilities.

The Tersoff-Munetoh potential utilizes a better motivated concept of 'bond order' for covalent materials. It means that the strength of a single chemical bond is affected by the chemical surrounding: the more neighbors an atom has, the weaker are the bonds which are formed to those atoms. Since for every larger number of bonds, each single bond has less pairs of electrons, it is natural that the strength of the individual bond decreases. The Tersoff-Munetoh potential is a cluster-functional and a pure bond order potential which has an environment dependence and no absolute minimum at the tetrahedral angle. Tersoff-like potentials have a generalized form:

$$V = V_{\text{repulsive}}(r_{ij}) + b_{ijk} V_{\text{attractive}}(r_{ij}) \tag{9}$$

Here the attractive and repulsive parts are essentially pair potentials, but the strength of the attractive part is affected by the environment through a coefficient b_{ijk}. As every Si potential must have some type of angular dependence, it is embedded inside the b_{ijk} environment-dependent term. Therefore, it does not result in a fixed minimum angle between bonds, which is good for predictability of new configurations that have not been used at the fitting stage.

In order to assess how well these potentials model the elastic properties, the Young's modulus for bulk crystalline silicon, α-quartz and amorphous SiO_2 were calculated. Three periodic bulk structures were created: a crystalline Si sample with a perfect diamond lattice, an α-quartz sample and an amorphous SiO_2 (silica) sample.

Though α-quartz and silica have the same chemical formulas, they have different structures and physical properties. In both compounds, Si atoms exhibit a tetrahedral coordination, with four oxygen atoms surrounding the central Si atom. α-quartz has a long range periodicity, the crystal lattice is trigonal, diamond-like, with Si atoms at the lattice position and an oxygen bridging each Si-Si unit. In contrast, silica does not preserve the long range order; nevertheless, oxygen atoms are sheared between two tetrahedrons and the structure generally does not contain many under or over coordinated atoms [76]. The 2D schematic projections of α-quartz and silica are presented in Fig. 6.

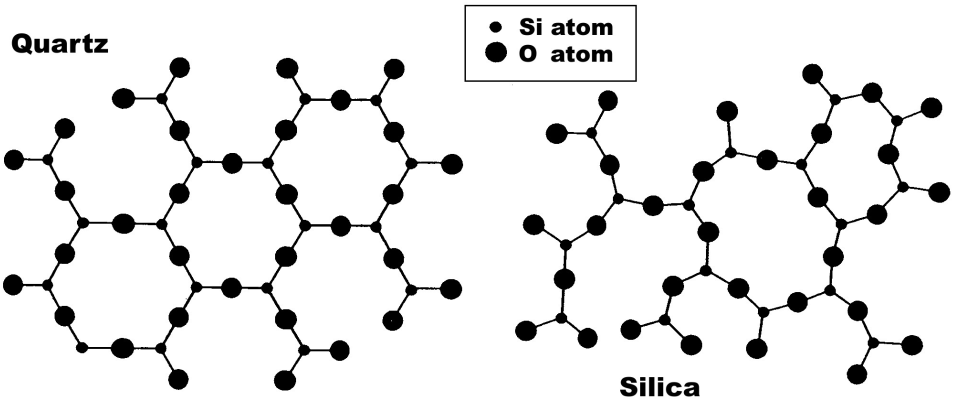

Figure 6: Schematic illustration of α-quartz and silica structural differences.

A realistic silica structure should consist of SiO_4 tetrahedrons connected in a random network. Because of the time limitation of the MD method, it seems to be barely possible to simulate a direct creation of silica samples by e.g. melting α-quartz and cooling it down. The simulated cooling rate is much higher than in a real experiment and the amount of coordination defects usually remains too high [77, 78]. The more effective computational approach is the Monte Carlo based Wooten, Winer and Weaire (WWW) algorithm [71, 79]. At the first stage of the algorithm, Si and oxygen atoms are arranged in α-quartz lattice. Subsequently, the network is randomized by bond-switch Monte Carlo moves which are either accepted or not, according to a rigid Keating potential [71]. After that, the structure can be optionally relaxed by the MD method using the desired potential in order to adjust the positions of atoms to be compatible with that certain potential.

In this work, the silica sample previously generated in our group by the means of WWW algorithm [77] was used. Bonding analysis of that sample has demonstrated that the generated random network remained essentially defect free; only a small fraction ($\approx 0.1\%$) of atoms had coordination defects [78].

The MD code PARCAS [42, 43] was used for the simulations. Before stretching, the samples were initially relaxed at 300 K for 60 ps by using the Berendsen thermostat described earlier. Periodic boundary conditions were applied in all directions and the Berendsen pressure control was activated to reduce the pressure along the x, y and z directions to zero. After the relaxation runs, the systems were first compressed and then stretched in small successive steps in order to determine the Young's modulus along the desired direction. Two other directions were still under the control of the Berendsen algorithm that removed extra pressure appearing during the deformation. The amount of deformation should be relatively small ($\leq 0.5\%$), so that the system stays in the elastic regime.

The elastic potential energy U_{e} of the system can be expressed as a function of the system length as

$$U_{\mathrm{e}} = \int \frac{EA_0 \Delta L}{L_0} d(\Delta L) = \frac{EA_0 \Delta L^2}{2L_0} \tag{10}$$

where E is the Young's modulus of the material, A_0 is the initial cross-sectional area, L_0 is the initial length, and $\Delta L = L - L_0$ is the amount by which the length was changed. When a second order polynomial:

$$U_e = aL^2 + bL + c \tag{11}$$

is fitted to the potential energy versus length dependence from stretching simulations, the Young's modulus can be obtained as:

$$E = -b/A_0 \tag{12}$$

The derivation of Eq. (12) is given in Ref. [80]. The results of the stretching simulations are presented in Table 1.

Material	$E_{\mathrm{Experimental}}$ (GPa)	$E_{\mathrm{Samela-Wat.}}$ (GPa)	$E_{\mathrm{Tersoff-Mun.}}$ (GPa)
Si [100]	130	77.9 ± 1.5	90 ± 2
Si [111]	189	122 ± 3	168 ± 4
α-quartz [100]	86	124 ± 3	66.4 ± 1.6
Silica	73	101 ± 1	45.0 ± 0.5

Table 1: Young's moduli of Si, α-Quartz, and silica along the specified directions. The experimental data [81], and the values calculated from MD simulations are presented. From Publication I.

The absolute values of the Young's modulus (Table 1) are significantly different when compared with the experimental values for the both potentials. However, when one compares the relative values, it becomes evident that the Tersoff-Munetoh potential predicts the same trend as the experimental results: silicon dioxide in the form of α-quartz is less stiff than crystalline silicon, and silica is less stiff than α-quartz. Particularly, the ratios of the Si [111] and silica Young's moduli are 2.6 and 3.7, as obtained from experiments and using the Tersoff potential, respectively. On the other hand, the Samela-Watanabe potential does not have the right order of the stiffness of the three materials.

Based on this, the Tersoff-Munetoh potential was selected to model the interactions between Si and O atoms as it represents the elastic properties of various Si-O systems more realistically.

The finite element calculations (described further) employed the complete elasticity matrix for Si; the matrix was evaluated using the script 'ELASTIC' by Thompson A. provided with the LAMMPS distribution. This script utilizes the conjugate-gradient energy minimization technique while distorting the system in different directions, to obtain the elastic energy as a function of various displacements. Poisson's ratio ν of silica had been estimated according to the change of the system size in the lateral directions during the stretching test described above. The results of these complementary tests are presented in Table 2.

Material	Parameter	$E_{\text{Experimental}}$ (GPa)	$E_{\text{Tersoff-Mun.}}$ (GPa)
Si	C_{11}	165.6	142.5
Si	C_{12}	64.0	75.4
Si	C_{44}	79.5	69
Silica	ν	0.17	0.22

Table 2: Elastic constants evaluated for the Tersoff-Munetoh potential. The experimental data [81] and values calculated from the MD simulations are presented.

4.3 Simulation setup

Si nanorods with axis along the [111] direction and facets of type [112] are studied within this work. It has been demonstrated that such a structure is the most stable one for small-diameter Si nanowires [82]. A bending force was applied by a diamond hemisphere with a 5 nm diameter. All atoms in the diamond tip were immobilized to simplify the calculations, representing an infinitely hard indenter. Interactions between C atoms of the indenter and Si and O atoms composing the nanorods were described by the purely repulsive Ziegler-Biersack-Littmark (ZBL) universal potential [45]. It has already been demonstrated that the lack of the attractive part in the ZBL potential does not influence the defect formation in nanowires, neither the force-deflection relationships during the compression phase [83]. However, it affects the position at which the stress induced by the indenter becomes tensile. Examples of the simulation setup are presented in Fig. 7.

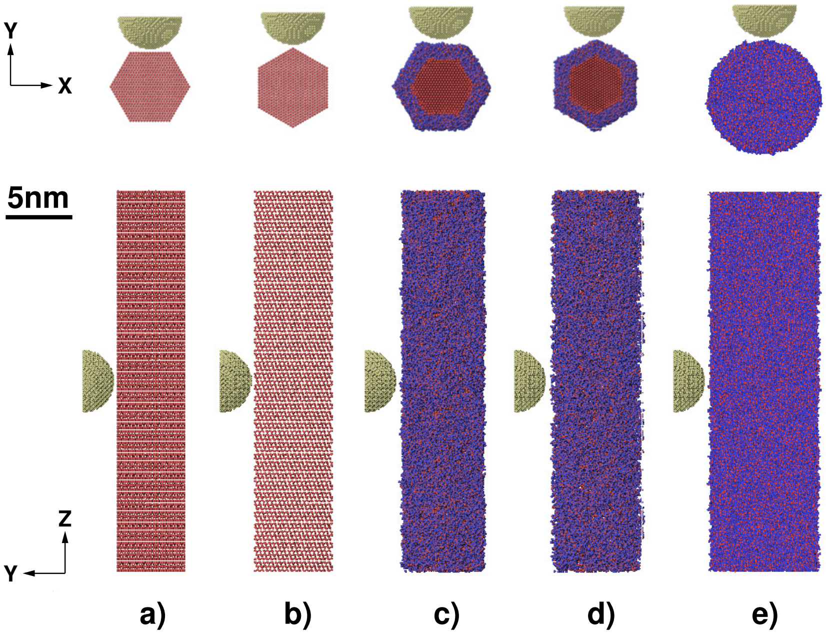

Figure 7: Simulation setup (nanorods of the smallest size): light gray hemisphere is a carbon nanoindenter; (a) is a pristine crystalline Si nanorod; (b) is (a) rotated 30° around its axis; (c) is a partially oxidized; (d) is (c) rotated 30° around its axis; (e) is a fully oxidized nanorod.

To test the influence of nanorod's orientation on the bending behavior, for the nanorods of the smallest size we prepared configurations where the nanorod was rotated 30° around its axis (Figs. 7b and 7d). To test the size related effects, we have prepared four sets of nanorods; nanorods from the first group had approximately the same length-to-diameter ratio, but a different scale: 5.8 × 31 nm, 7.9 × 46 nm, and 10.4 × 62 nm (sizes in the pristine state). The nanorod from the second group, in which the shear effects are less exposed during bending tests, had the size of 5.8 × 63 nm.

The bending simulations were done in a quasistatic manner, i.e. the system was initially relaxed, then the indenter was moved towards the surface by 0.01 nm, the system was relaxed in such position and the forces were recorded, and so on. The system temperature was maintained at 300 K using the Berendsen temperature control [37]. To imitate the clamped ends boundary conditions, two atomic layers at the ends of the nanorods were immobilized. As the border atoms were fixed, any rotations and shifting of the nanorods were prevented, though in a real experiment the boundary conditions might be less perfect, which results in additional errors [62].

4.4 Creation of the oxide layer

The most realistic approach to model a native oxide formation would be to simulate nanorods in an oxygen atmosphere and let the oxidation happen until the saturation is reached. It has been demonstrated by Khalilov et al. [84] that such simulations are in principle possible with the ReaxFF force field. However, the time limitation of MD method does not let to simulate oxidation with a standard ambient pressure and temperature. Importantly, when the oxide layer is formed artificially by e.g. the hyperthermal oxidation, the oxide thickness and structure, as well as the interface properties may differ significantly from those of a native oxide [85–87].

The approach used in this work for creating oxidized nanorods was to assemble them from the pristine Si and the silicon dioxide materials in core-shell structures, and relax the interface by annealing. The thickness of the silica shell was selected to be 1 nm for all structures. Such a silica thickness should reasonably represent the native oxide appearing in air at standard ambient temperature and pressure [88]. Of course, the question of what the native oxide thickness should be in the case of nanowires is still arguable, as the value given above was measured for the bulk material. The geometrical parameters of the cores and the shells were selected in such a way, that the amount of Si atoms was roughly the same as for the pristine Si nanorods; this should mimic how a native Si oxide is formed in air, when oxygen diffuses into Si while the number of Si atoms does not change. The shells of desired shape were cut from the bulk silica sample generated by the WWW algorithm described earlier in Section 4.2. The cores and the shells were relaxed separately at 300 K with the Berendsen pressure control applied along the nanowires' axes. Afterwards, the atomic coordinates of the crystalline cores in the cross-sectional plane were scaled by a factor 0.98 (i.e. compressed) and inserted inside the shells, to avoid the unphysically short bond distances between the core and the shell atoms during the initial relaxation.

It has been demonstrated that such a technique results in a realistic interface with a small number of coordination defects after annealing [78].

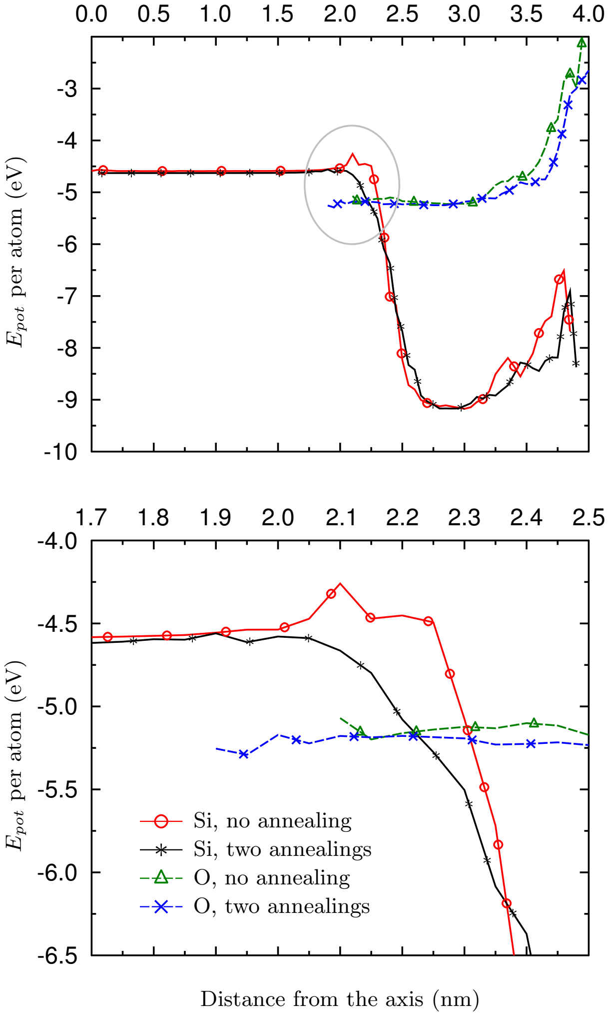

Figure 8: Potential energy of atoms in the 5.8×31 nm oxidized nanorod as a function of the radial distance from the nanorod axis, before and after annealing. The lower plot represents the area highlighted by the circle on the upper plot. From Publication II.

Interface optimization was done by quick heating the system up to 1250 K and then 'slow' cooling down to 0 K during 50 ps, repeated 3 times. The average potential energy per atom as a function of distance from the nanowire axis is presented in Fig. 8. The additional potential energy of Si atoms near the interface has disappeared after the second annealing, indicating that the interface is sufficiently relaxed.

Additionally, silica nanowires with the same length and the same amount of Si atoms were created to investigate the complete oxidation state. They were not annealed but just relaxed at 300 K using the Berendsen temperature control.

4.5 Analysis of stress

Shi et al. has demonstrated [89] that residual stresses in beams directly influence the bending stiffness due to the geometrical nonlinearity of finite deformations and the Poisson's effect, leading to different moments acting on upper and lower parts of the beams even if the residual stresses are symmetrical with respect to the axis. So, in order to make FEM simulations more realistic by introducing surface stresses, we have calculated stresses in the nanorods from the MD simulations. The average components of the stress tensor as a function of the radial distance from the nanorod axis (the z axis of the coordinate system) are presented in Figs. 9 and 10.

In Fig. 9 we can observe that for the pristine Si nanorods of all sizes, the surface stress is almost the same independently on the radius, but for the biggest nanorod, the hoop $\sigma_{\theta\theta}$ and the radial σ_{rr} stresses induced in the inner layers are approximately twice smaller; this is reasonable as the surface stress encloses the bigger inner volume in this case. The off-diagonal stress tensor components $\sigma_{r\theta}, \sigma_{\theta z}$ have not had any distinguishable values at the surface in comparison with the inner layers, and were about two orders of magnitude smaller than σ_{rz} which is presented on the plot. Thus, we ignored $\sigma_{r\theta}$ and $\sigma_{\theta z}$ in the FEM calculations. One should have in mind that the stress distribution is not very smooth, as the nanorods had a hexagonal cross section and the plot is made as a function of a radial distance, which perfectly suits only cylindrical shapes.

The influence of oxidation on the stress distribution is demonstrated in Fig. 10. The stress tensor components of the fully oxidized nanorod fluctuate around zero due to its disordered amorphous structure, and only σ_{rr} has a distinguishable value of 6 GPa near the surface. The σ_{rr} component of the partially oxidized nanorod behaves similarly as that of the pristine one, but the values are reduced by 1.5 GPa due to the lower surface stress on the amorphous oxide layer; σ_{rr} within the inner layers becomes compressive (negative) due to the influence of the oxide shell. The hoop $\sigma_{\theta\theta}$ and the longitudal σ_{zz} stress tensor components also invert their sign and become tensile in the oxidized shell and compressive in the Si core. It has been observed recently during the MD studies of oxidation of Si nanowires [84, 90, 91] that a large compressive radial stress is induced in a Si core during the oxidation process, due to the difference in the atomic volumes of Si and silica. One should, however, note that in those works the oxide layers were created by the hyperthermal growth process contrary to our study, where the nanorods were built by cutting from a bulk and subsequently relaxed. In our simulations it is possible to modify the shell stresses directly by changing the geometrical parameters of the core-shell structure during the assembly stage.

4.6 Tensile tests

The simplest method to calculate the Young's modulus of a nanorod by MD is to perform a tensile test, described in detail in Section 4.2. The only difference is that in case of a nanorod we did not perform the compression stage (as a nanorod may buckle), and

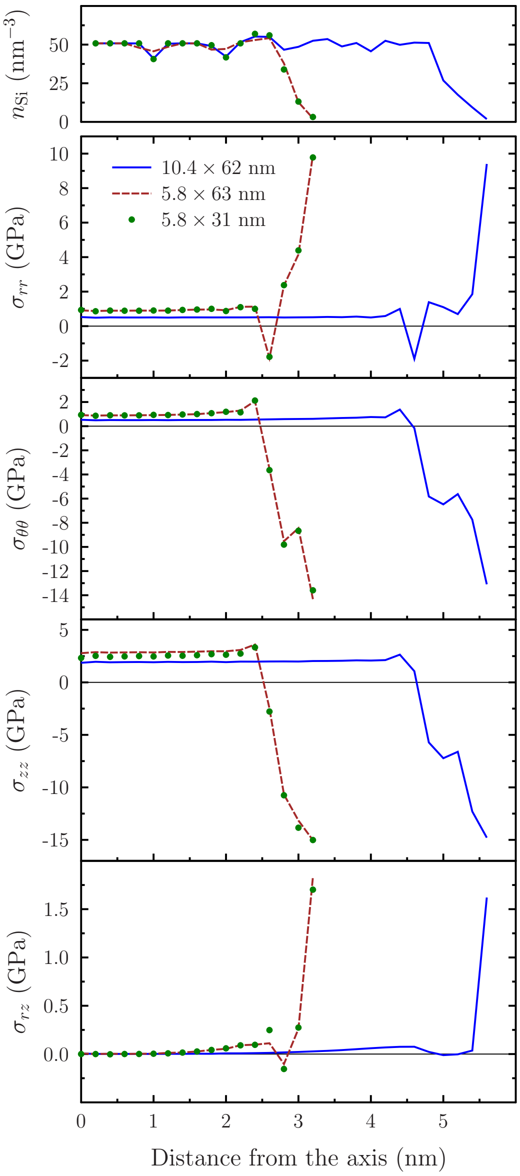

Figure 9: Components of the stress tensor for Si nanorods of various sizes in the cylindrical coordinate system, as a function of the radial distance from the nanorod axis, calculated by MD. The upper subplot shows the radial density of Si atoms. From Publication IV.

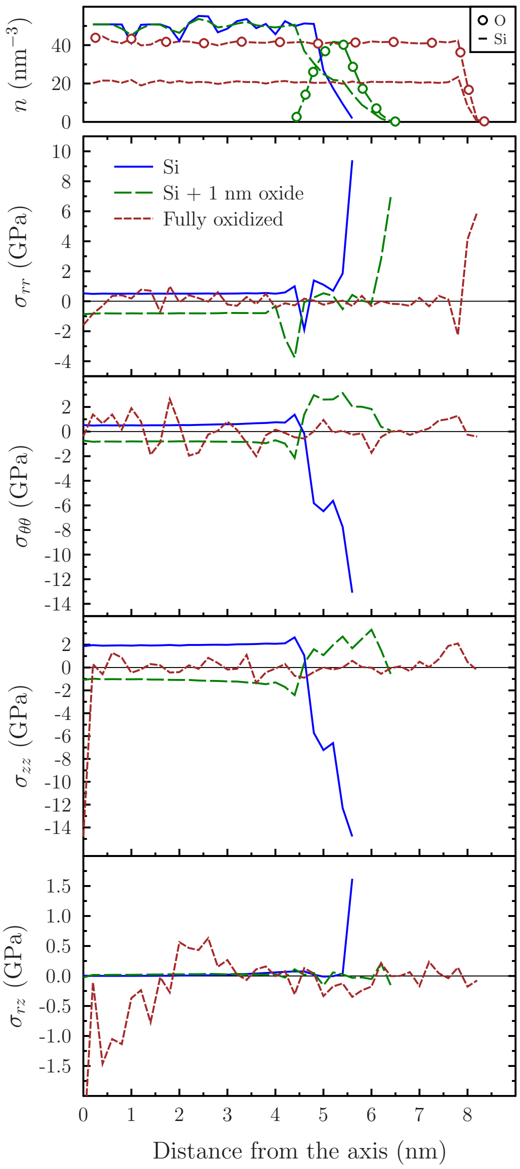

Figure 10: Stress tensor components of the 10.4 × 62 nm nanorod depending on the oxidation level in the cylindrical coordinate system, as a function of the radial distance from the nanorod axis, calculated by MD. The upper subplot shows the radial densities of Si and O atoms. From Publication IV.

the periodic boundary conditions were applied exclusively along the axis. To calculate the Young's modulus E from simple stretching simulations, we have fitted a second order polynomial to the elastic energy versus length dependence, as was described above. Young's modulus as a function of the oxide thickness is presented in Fig. 11. We have also fitted a simple core-shell model [21] using the bulk Young's modulus values obtained by MD calculations with the Tersoff Si-O potential ($E_{\mathrm{Si}} = 168 \pm 4$ GPa for Si [111] and $E_{\mathrm{silica}} = 45 \pm 1$ GPa for silica, respectively). According to this model, an oxidized nanorod consists of a core with elastic modulus E_{Si} and an oxide shell with elastic modulus E_{silica}. Under tension, the Young's modulus E of the nanorod can be calculated as

$$E = E_{\text{Si}}\left[1 + 4\left(\frac{E_{\text{silica}}}{E_{\text{Si}}} - 1\right)\left(\frac{t_{\text{oxide}}}{2R} - \frac{{t_{\text{oxide}}}^2}{4R^2}\right)\right] \tag{13}$$

where R is the radius of the circular cross section and t_{oxide} stays for the oxide thickness. Hence, the Young's modulus of the nanorod in this model is calculated as a weighted average of the Young's moduli of the core and the shell materials, depending on the area occupied in the cross-section. Eq. 13 applies equally to nanorods with a hexagonal cross section, assuming R as a hexagon side length and t_{oxide} as a shell thickness along a vertex.

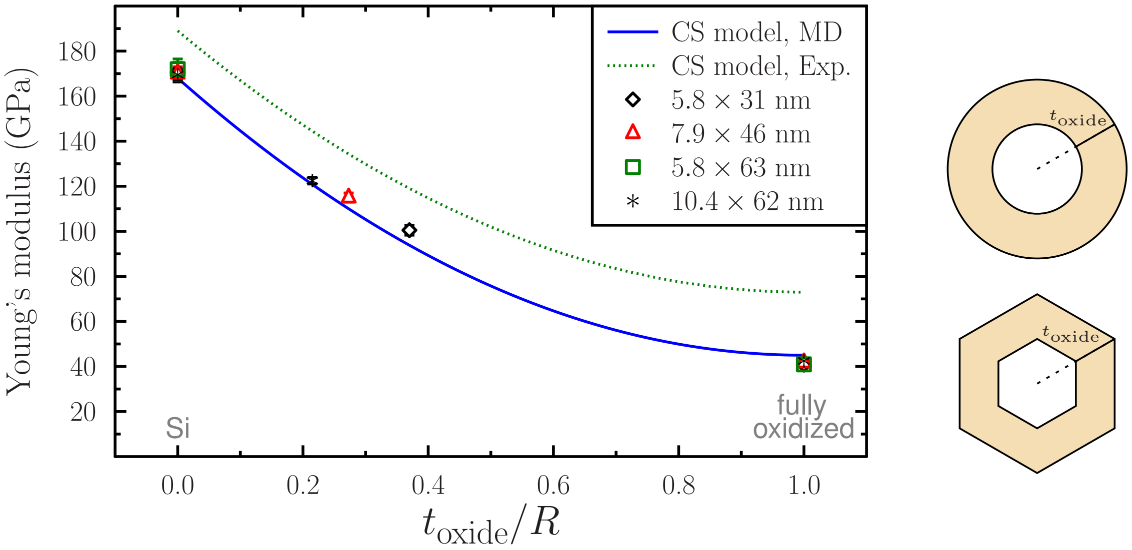

Figure 11: Young's moduli of Si nanorods of various sizes, as a function of the oxidation level. The values from the tensile MD calculations are highlighted by markers; 'CS model, MD' denotes the values predicted by the core-shell model where the elastic constants obtained from the MD bulk simulations were used, and 'CS model, Exp.' denotes the model incorporating the real experimental values [81]. From Publication IV.

The results of the MD calculations demonstrate a good agreement with the core-shell model. The pristine Si and the purely oxidized silica nanorods had the same Young's moduli values as the simulated bulk materials [Publication **II**], independently on their size. However, the obtained results are underestimated in comparison with the experimentally measured Young's modulus values, and depend on the potential used. Thus, the increased surface to volume ratio in case of the nanorods having smaller diameters did not play any significant role when tensile tests were preformed along nanorod axis.

4.7 Three point bending tests

In order to remove the indentation effect of the diamond tip, two series of simulations were carried out. During the first series, nanorods were immobilized only at the ends ('bending' with deflection δ_b). During the second series, nanorods were additionally immobilized at the very bottom, as if they were lying on an infinitely hard substrate ('indentation' with deflection δ_i); both cases are presented in Fig. 12.

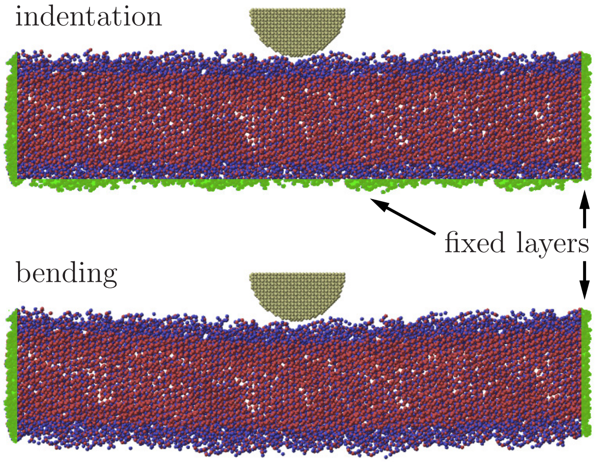

Figure 12: Bending and indentation simulation schemes; layers highlighted in green were immobilized during the simulations.

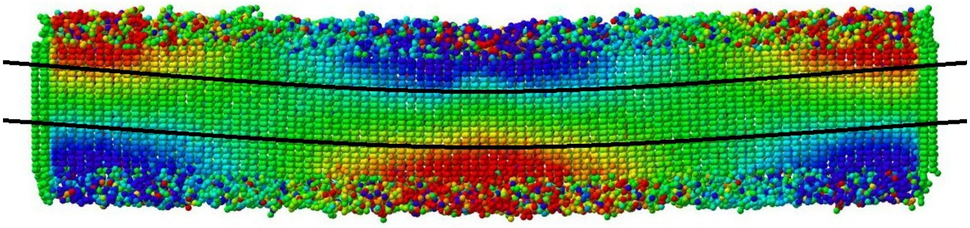

Figure 13: Axial strain inside the bent nanowire; red color denotes stretched layers, blue - compressed, and green areas are undeformed; in arbitrary units

To obtain a pure bending displacement (deflection δ_pb), we have subtracted indentation displacements from bending displacements for the same force F values [63]:

$$\delta_\mathrm{pb}(F) = \delta_\mathrm{b}(F) - \delta_\mathrm{i}(F) \tag{14}$$

From the pure bending deflection, the effective bending modulus $E_\mathrm{b.eff.}$ of a nanorod can be calculated. For a beam having both ends fixed, $E_\mathrm{b.eff.}$ is expressed as [18, 93]

$$E_\mathrm{b.eff.} = (\frac{F}{\delta_\mathrm{pb}})\frac{L^3}{192I} \tag{15}$$

where I is the second area moment of the nanorod cross-section, L is the nanorod length. (F/δ_pb) is a linear coefficient obtained when a linear function is fitted to the pure bending force-deflection dependence. For nanorods with a hexagonal cross-section the second area moment is defined as

$$I_{\text{hex}} = \frac{5\sqrt{3}}{16}a^4 \tag{16}$$

where a is a hexagon side length. For cylindrical nanorods

$$I_{\text{cyl}} = \frac{\pi}{4}R^4 \tag{17}$$

where R is a cylinder radius. Note that for cylindrical and hexagonal shapes having the same cross sectional area, the second area moments are also quite close to each other

$$\frac{I_{\text{hex}}}{I_{\text{cyl}}} = \frac{5\sqrt{3}\pi}{27} \approx 1.008 \tag{18}$$

implying that the exact shape of the nanorod does not have significant influence on the bending properties.

One should remember, that $E_{\text{b.eff.}}$ calculated from Eq. 15 corresponds to the Young's modulus only if a nanowire has a sufficiently big length-to-diameter ratio ($\geq$ 20), as was explained in Section 4.1. For short nanorods, the contribution of shear deformations becomes significant, which is demonstrated in Fig. 13. Here one can see, that the opposite layers at the middle of the nanorod and also near the ends have a different sign of the longitudinal strain, resulting in a shear strain between the neighboring layers (as the imaginary layers are rigidly connected together making up the entire structure).

4.8 Finite Element Modeling of the three point bending tests

In order to estimate how well the continuum mechanics approach can describe the bending behavior of nanowires, MD simulations have been accompanied by finite element modeling (FEM) of nanorods with the same geometry.

FEM is a numerical method for finding approximate solutions to boundary value problems described by partial differential equations. In FEM, the whole system is divided to a set of small regions of a simple shape - finite elements, interconnected at points called nodes. After that, variational methods are used to solve the problem by approximating it with local shape functions defined for the finite elements, and subsequently minimizing an associated error function. In structural mechanics, the physical properties of the bulk material such as thickness, density, Young's modulus, shear modulus and Poisson's ratio (or the elasticity matrix in case of anisotropic material) are assigned to the elements.

The finite element approximation results in a system of equations relating the initial boundary conditions at the nodes to the unknown variables at the same nodes. The contribution of each element is computed from the local stiffness matrix $\mathbf{K}_m$. The equations can then be written in the matrix form as $\mathbf{Ku} = \mathbf{f}$, where $\mathbf{u}$ is the vector of unknown nodal variables, $\mathbf{f}$ is the vector of external forces, and $\mathbf{K}$ is a global stiffness matrix assembled from $\mathbf{K}_m$ of individual elements. The total energy function $E(\mathbf{u})$ of a system consisting of a linear elastic body Ω and external forces $\mathbf{f}$ applied to the boundary Γ can be expressed as a combination of the strain energy and the work produced by $\mathbf{f}$

$$E(\mathbf{u}) = \frac{1}{2} \int_{\Omega} \mathbf{u}^T \mathbf{B}^T \mathbf{C} \mathbf{B} \mathbf{u} \, \mathrm{d}X - \int_{\Gamma} \mathbf{f}^T \mathbf{u} \, \mathrm{d}X \tag{19}$$

where $\mathbf{B}$ is the strain-displacement matrix, and $\mathbf{C}$ is the matrix of elastic constants. The goal of the finite element method is to find such values of $\mathbf{u}$ which minimize the function $E(\mathbf{u})$. To do that, the strain energy from $E(\mathbf{u})$ is approximated with the local matrices $\mathbf{K}_m$ of the finite elements, the global system of equations for all elements is assembled, and the nodal variables $\mathbf{u}$ are resolved. In the aforementioned case of a mechanical problem, $\mathbf{u}$ corresponds to displacements of the nodal points. Unknown physical properties of the finite elements like strains or stress can then be determined using the displacement field. More details about the method can be found in e.g. [94].

The simulation software COMSOL 4 Multiphysics [95] was used to setup the models, do meshing and perform computations. The schematic setup is presented in Fig. 14.

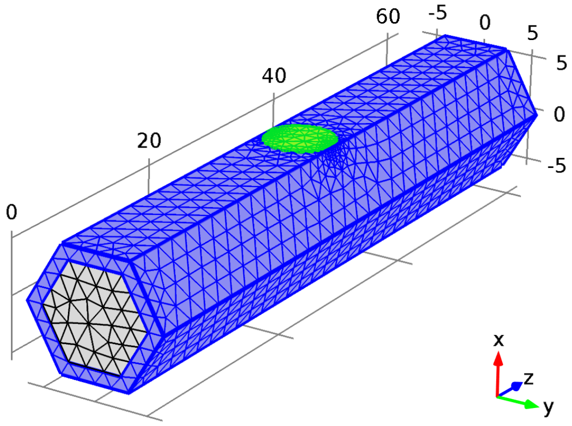

Figure 14: The FEM model of the three point bending of the partially oxidized nanorod. The Si core is marked in gray, while the silica oxide shell is displayed in blue. The bending force was applied to the green circular area in the middle of the upper face. The ends of the nanorod were fixed. The bottom was either fixed or not, to get the pure bending displacement.

We used the Structural Mechanics Module with the Solid Mechanics interface, which calculates displacements under the prescribed boundary conditions by solving the complete Navier's equations. Anisotropic effects in the Si core were taken into account, and the crystal lattice was oriented in the same way as in our MD calculations. The core and the shell were rigidly coupled, and tetrahedral elements were used in meshing. The calculations were performed for displacements smaller than 1%. Force was applied to a circular area; we have verified that while varying the area over which the force is applied, the pure bending displacement remained practically the same. The experimental material elastic constants provided within COMSOL were used, and for the sake of comparison we additionally performed some of the calculations using elastic moduli obtained from MD (Section 4.2).

4.9 Results

The examples of the force-deflection relationship for the bending and indentation simulations (the smallest 5.8×31 nm pristine and partially oxidized nanorods) are presented in Fig. 15. The pure bending curves obtained by subtracting the indentation data from the bending data are demonstrated in the same plot as well. They are supposed to behave linear according to Eq. 15. To verify that quantitatively, an arbitrary power functions of the form ($F(\delta) = a(\delta - b)^c$) were fitted to the pure bending data. The fitting resulted in the values for the exponent c as 1.02 ± 0.03, 0.99 ± 0.07, 1.05 ± 0.07, and 1.00 ± 0.04 for the cases (a), (b), (c), and (d), respectively (see Fig. 7). Therefore, a simple linear function was used for fitting of the pure bending data during the bending modulus calculations.

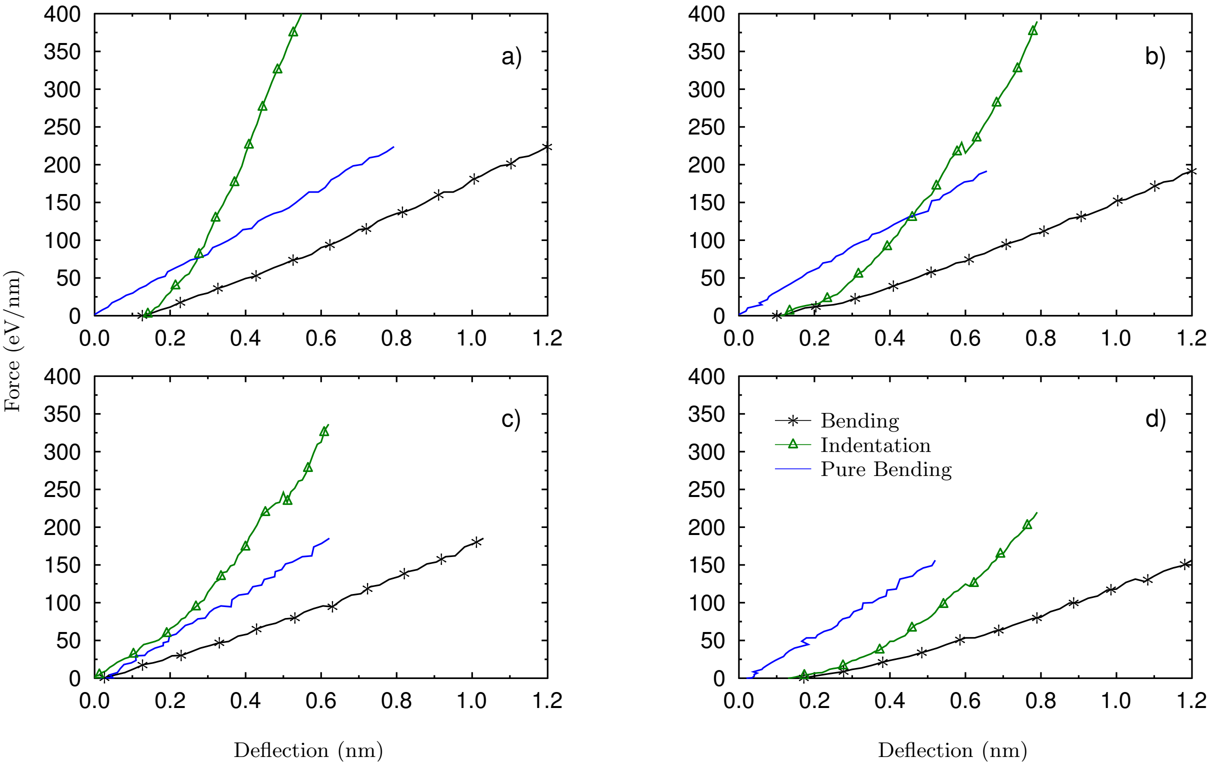

Figure 15: Force-deflection curves for the 5.8×31 nm nanorod. Subplots labeling matches the simulation setups shown in Fig. 7. From Publication I.

The effective bending moduli $E_{\text{b.eff.}}$ values calculated from the pure bending displacements δ_{pb} using Eq. 15 are presented in Figs. 16 and 17, and also in Table 3. To introduce surface stresses to the FEM models of the pristine and completely oxidized silica nanorods, 0.05 nm thick outermost layer was sacrificed for the 'surface', and the components σ_{rr},$\sigma_{\theta\theta}$,σ_{zz}, and σ_{rz} of the stress tensor calculated by MD were assigned for that layer. For the partially oxidized Si nanorods, σ_{rr} was assigned only for the 'surface', while $\sigma_{\theta\theta}$ and σ_{zz} were assigned to the entire oxide shell, in accordance to our MD simulations.

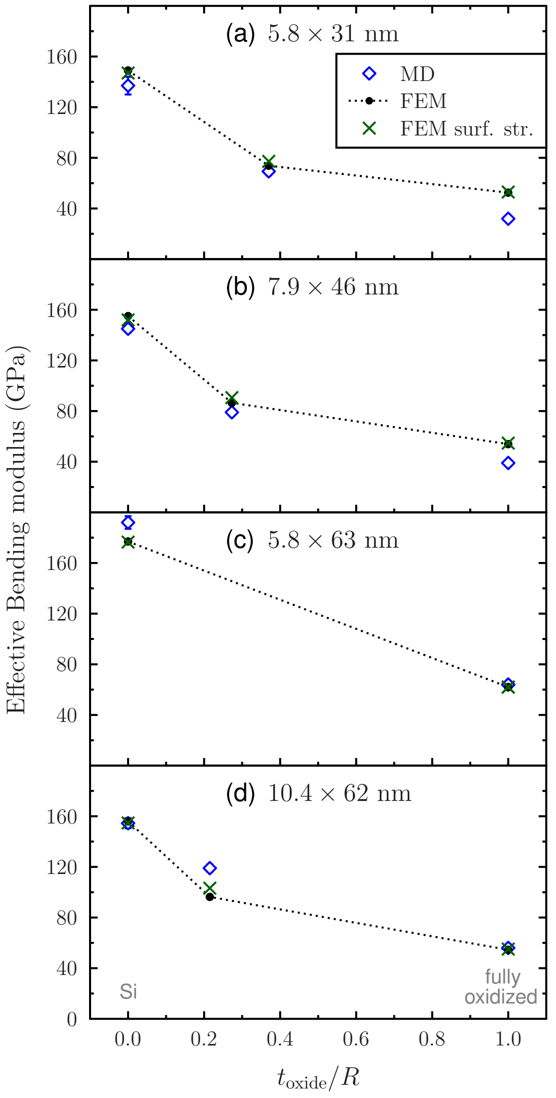

Figure 16: Effective bending modulus of nanorods calculated by MD, and by FEM with and without taking into account the surface stresses; as a function of the oxidation level. The experimental elastic constants were used for both of the presented FEM calculations. From Publication IV.

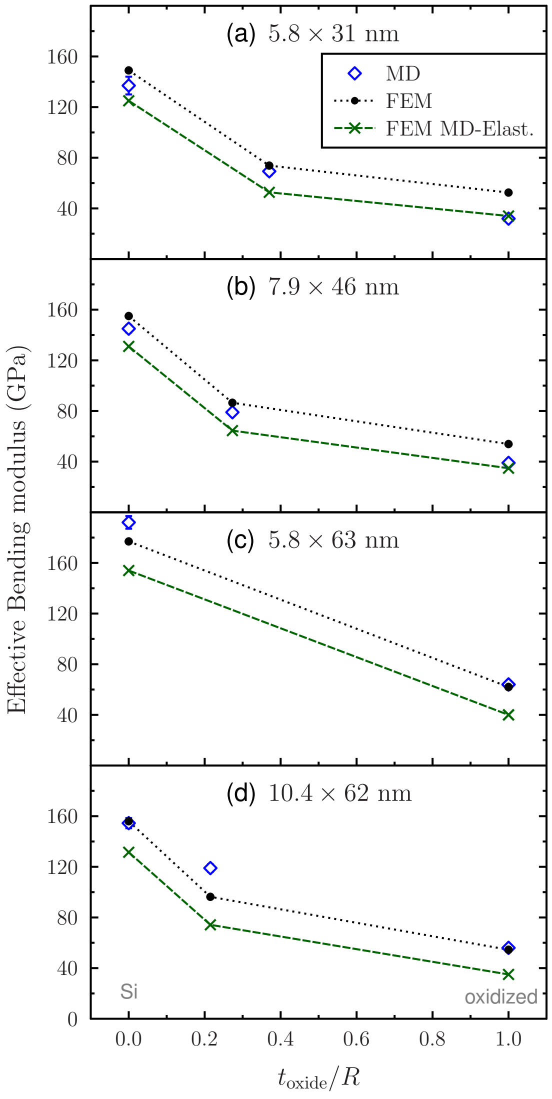

Figure 17: Effective bending modulus of nanorods calculated by MD, by FEM with the experimental elastic constants, and by FEM using the elasticity matrix determined by the bulk MD calculations with the Tersoff-Munetoh potential; as a function of the oxidation level. The surface stresses were taken into account in both of the presented FEM calculations.

FEM results for the nanorod models where intrinsic stresses were not taken into account are also presented for the sake of comparison in Fig. 16. The comparison of the results from the FEM simulations using the experimental elastic constants of Si and silica predefined in COMSOL, and then the elastic constants calculated by MD for the Tersoff Si-O

t_{oxide}/R	D (nm)	L/D	E_{MD} (GPa)	E_{FEM} (GPa)	$E_{\mathrm{FEM}}/E_{\mathrm{MD}}$	$E_{\mathrm{FEM'}}$ (GPa)	$E_{\mathrm{FEM'}}/E_{\mathrm{MD}}$
Results for 5.8 × 31 nm nanorod							
0.00	5.8	5.3	137.0 ± 7	149.0	1.09 ± 0.06	147.0	1.08 ± 0.06
0.00^*	5.8	5.3	141.0 ± 7	-	-	-	-
0.37	7.1	4.4	69.3 ± 3	73.8	1.07 ± 0.05	77.2	1.12 ± 0.05
0.37^*	7.1	4.4	71.5 ± 3	-	-	-	-
1.00	9.4	3.3	31.9 ± 1	52.5	1.65 ± 0.05	53.0	1.66 ± 0.05
Results for 7.9 × 46 nm nanorod							
0.00	7.9	5.9	145.0 ± 3	155.0	1.07 ± 0.02	152.0	1.05 ± 0.02
0.27	9.6	4.8	79.0 ± 2.5	86.5	1.10 ± 0.03	90.6	1.15 ± 0.04
1.00	12.5	3.7	39.0 ± 1	53.9	1.38 ± 0.04	54.7	1.40 ± 0.04
Results for 5.8 × 63 nm nanorod							
0.00	5.8	10.8	192.0 ± 5	177.0	0.92 ± 0.02	176.5	0.92 ± 0.02
1.00	9.3	6.7	64.0 ± 2	62.0	0.97 ± 0.03	62.0	0.97 ± 0.03
Results for 10.4 × 62 nm nanorod							
0.00	10.4	6.0	154.5 ± 4	156.0	1.01 ± 0.03	154.7	1.00 ± 0.03
0.22	12.2	5.1	119.0 ± 3	96.3	0.81 ± 0.02	103.2	0.87 ± 0.02
1.00	16.3	3.8	56.0 ± 1	54.5	0.97 ± 0.02	55.1	0.98 ± 0.02

Table 3: Effective bending moduli values calculated by the MD and the FEM methods. $E_{\mathrm{FEM'}}$ denotes the results of the FEM calculations with the surface stresses included; E_{FEM} is without. For cases 0.00^* and 0.37^*, the nanorod was rotated in such a way, that the indenter was opposed to the edge (shown on Figs. 7a and 7c). The errors for the MD values are estimated from inaccuracies of the size measurements as well as the linear fitting. The data is from Publications I and IV.

potential is demonstrated in Fig. 17. The differences between the FEM and MD results (for the FEM simulations done with the predefined elastic constants) are listed in Table 3. All but two cases (except the lines 0.00^* and 0.37^* in Table 3) concern orientation of the nanorods with respect to the indenter presented in Fig. 7a and Fig. 7c (i.e. when the indenter interacts with a facet of the nanorod).

The relative differences between the FEM and the MD results are quite consistent for the pristine and the partially oxidized nanorods, and span from 5 to 15 % with the exception of the 10.4 × 62 nm partially oxidized nanorod (Table 3). At the same time, the fully oxidized 5.8 × 31 nm and the 7.9 × 46 nm silica nanorods show a significant size dependence with smaller actual $E_{\mathrm{b.eff.}}$ than was predicted by FEM. From Fig. 11 it is evident that the Young's moduli are same for all silica nanorods independently of their radii, and consequently the observed difference must be attributed to the shear modulus deviations. Indeed, the 5.8 × 63 nm silica nanorod has the smallest difference between the $E_{\mathrm{b.eff.}}$ FEM and the $E_{\mathrm{b.eff.}}$ MD values and has the negligible contribution of shear deformations (see Section 4.1). This agrees with the model suggested by Cohen et al. [96], who demonstrated that shear modulus drops significantly when the diameter of a beam is reduced for nanosized amorphous beams. This happens due to the increased contribution of surface particles with a bigger degree of freedom, whereas for monocrystalline beams such an effect is much less notable.

The inclusion of the surface stresses to the FEM model does not change significantly $E_{\mathrm{b.eff.}}$

values neither for the pristine nor for the fully oxidized nanorods. On the other hand, defining the $\sigma_{\theta\theta}$ and σ_{zz} components for the oxide shell increases the predicted $E_{\text{b.eff.}}$ values for the partially oxidized nanorods by $\approx 5-10\%$. Note, that the stresses in the oxide shell may be different from a real nanowire, as we have not simulated the oxidation process as it happens in reality but instead combined the Si cores and the silica shells and annealed (relaxed) the structures. To test how the bending properties of a partially oxidized nanorod may change in the presence of a compressive σ_{rr} component within the oxide layer, as was observed in [84, 90, 91], $\sigma_{rr} = -3$GPa was additionally assigned to the entire oxide shell in the FEM model of the 5.8×31 nm nanorod. Such a modification has increased $E_{\text{b.eff.}}$ value by 7 %. Thus, we can conclude that it is important to take into account the initial stresses, but one needs to know the exact stress tensor field for the analyzed system in order to get an accurate estimation.

The differences between $E_{\text{b.eff.}}$ obtained from the bending simulations where the nanowire was rotated 30° around its axis (cases 0.00^* and 0.37^* of the 5.8×31 nm nanorod), and the simulations with the ordinary orientation, seem to be negligible in comparison with the error bars, even for the crystalline Si nanorod. Of course, the stress concentration is higher when the indenter interacts with the edge of the nanorod, and it is expected to be important when the load is high enough and the deformations become plastic. But for the elastic regime, due to the nature of the bending deformation, the rotation of the nanowire around its axis should not affect the pure bending behavior when the indentation effect is removed, and if the boundary conditions are preserved (which is very hard to achieve in a real experiment).

Fig. 17 demonstrates a similar shift of the 'analytical' predictions (FEM in this case) when the bulk elastic constants estimated by MD were used instead of the real experimental constants, as was observed earlier in the core-shell model used for the tension test (see Fig. 11). The shift is by ≈ 15 GPa and almost the same for all tested nanorods independently on their oxidation level. When we take that into account and compare $E_{\text{b.eff.}}$ values between the MD results and the FEM results with MD elasticity, all our previous observations remain valid, with the only difference that all nanowires show some stiffening over the FEM predictions. This can be explained by the fact that elastic properties of the surface region are usually different due to the surface reconstruction and coordination defects [61], which was not taken into account in our FEM model (only the surface stresses were implemented). Moreover, even the MD results may be not entirely correct, as the classical MD simulations do not take into account the electronic density redistribution at the surface [97]; this is discussed deeper in Section 6. However, surface effects are shown to be less important during the axial load [98], which agrees with our results from the stretching simulations, where the observed Young's moduli were practically the same as those of the bulk materials.

5 Xe irradiation of Au nanorods

5.1 Irradiation experiment

In Section 3.2 we described the mechanism of collision cascades, which might happen when a high energy ion hits an object. It is also possible, that some of the recoil atoms reach the surface, if their energy at that moment is still bigger than the surface binding energy, they are ejected from the object permanently. Such atoms are called sputtered. If the material that is irradiated by heavy ions having energies in keV - MeV range is a dense but soft metal with a low melting temperature (like gold or lead), the thermal spike events become very probable. They can also be formed near the surface region, and when such a spike consisting of essentially molten material intersects with the surface, large numbers of atoms may sputter due to liquid flow processes and microexplosions [99, 100]. The surface damage to the object is very significant in this case and may include formation of craters and protrusions with sizes up to 10 nm [101, 102] for flat Au surfaces. It is reasonable to assume, that if one irradiates nanoobjects like nanoclusters or nanorods with dimensions of the same order of magnitude as a range of ions for that material, the probability of a thermal spike to intersect the surface should be enhanced [103]. Indeed, the surface-to-volume ratio is bigger for nanostructures, and the spike has a possibility to intersect with not only the top surface (on which the ion impacts), but also the side and bottom surfaces. However, one should remember, that there are some other factors that may significantly affect sputtering and damage production, e.g., nanostructures may have different cooling conditions, and the probability that the incoming ion or a high energy recoil leaves the nanoobject without producing successive collisions is higher due to the limited volume of the system. Also, the decreased melting temperature may become important for nanoparticles having radii ≤ 30 nm [104]. As the size of a thermal spike is typically in the nanometer range, it is interesting to analyze the question of whether ion-irradiation of nanostructures may significantly enhance the sputtering or not.

Recent experiments has demonstrated that under 80 keV Xe^+ ion irradiation of monocrystalline Au nanorods, the observed sputtered yields S, i.e. the total amount of material sputtered from an object after an ion impact, were in the range of 100-1900 atoms per ion [Publication **I**]. This is up to 10 times bigger than the expected yields from a planar Au surface under the same conditions, even taking into account the higher yield values for off-normal incidence [105, 106]. The nanowires were produced by electrodeposition of Au into the anodic Al_2O_3 porous template; the diameter of pores was 20 nm. At later stages, the template was dissolved and the nanowires were deposited onto Formvar-coated Cu transmission electron microscopy (TEM) grids. The analysis done by TEM and the diffraction methods showed that the produced nanowires were approximately 20 nm in diameter, about several microns in length, and consisted of columnar grains on the order of 100 nm in length along the wire, without any predominating growth direction. The samples were irradiated at the room temperature, and the ion beam was directed at 30° with respect to the electron beam, perpendicular to the nanowire axis. The evolution of one of the nanorods that produced the highest sputtering yield is presented in Fig. 18.

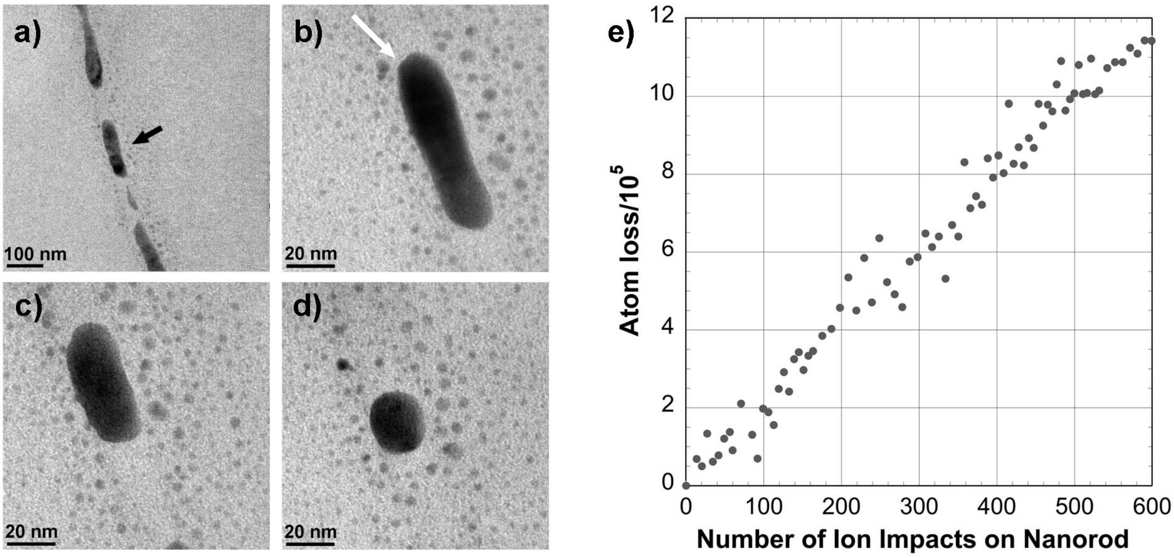

Figure 18: Changes to Au nanowire under 80 keV Xe$^+$ ion irradiation, bright field TEM images. (a) Segmentation of the nanowire at grain boundaries after 2.1×10^{14} ion/cm^2 fluence; (b) Selected nanorod before the additional irradiation, starting point for volume measurements; (c) Nanorod after additional ≈ 227 impacts, or 1.6×10^{13} ion/cm^2 fluence; (d) Nanorod after additional ≈ 316 impacts, or 5.5×10^{13} ion/cm^2 fluence; (e) Atom loss versus ion impacts for the nanorod shown on subfigures (b)-(d). From Publication I.

At the beginning of the experiment, after the fluence of 2.1×10^{14} ion/cm^2, the nanowire separated at the grain boundaries due to flow and sputtering processes (Fig. 18a). The produced smaller nanorods were then irradiated further. The diffraction measurements, conducted throughout the experiment, always showed a good contrast indicating that the nanorods remained overall solid during irradiation. For two nanorods, a series of images obtained from different tilt angles around the axis of the nanorod confirmed, that they retained a cylindrical shape even after numerous impacts. In Figs. 18 (b)-(d) we can observe the evolution of an individual nanorod following ≈ 540 impacts, the major length decreases almost transforming the nanorod into a spherical particle.

To evaluate the sputtering yields, the change in volume V was estimated according to geometrical measurements of the radius r_i at small successive $\Delta x_i \approx 0.46$ nm steps from the TEM images, assuming that the nanorod is cylindrical

$$V = \sum_i \pi r_i^2 \Delta x_i \tag{20}$$

The number of atoms in the nanorod was then calculated as the volume multiplied by the atomic density of gold (58.98 atoms/nm^3). The number of ions that impact on the nanorod was determined from the fluence and the projected area of the nanorod, with a trigonometric correction for the angle between the nanorod axis and the ion beam.

The measured yields S for four different irradiated nanorods were 823 ± 85, 1036 ± 87, 175 ± 21, and 147 ± 12 atoms per ion; such values could not be explained by the classical ballistic and evaporative sputtering models [Publication **I**], and the MD method was used to investigate this non-linear sputtering phenomena.

5.2 Simulation setup

MD simulations were performed in order to investigate the sputtering processes with an atomic resolution and to better understand the reasons for the high yields. An Au nanorod with dimensions typical of those used in the real experiment, i.e. 70 nm in length and 20 nm in diameter - 50 nm cylinder with hemispherical ends, was irradiated sequentially by individual 80 keV Xe ions.

The special features that should be introduced to the classical MD algorithm in order to simulate high energy ion impacts have been described earlier in Section 3.2. Interactions between Au atoms were modeled with the Foiles et al. EAM potential [107].

The Embedded Atom Method (EAM) is a formalism suitable for describing atomic interactions for most metallic systems [108]. This formalism is based on the effective medium theory; the real material is imagined to be replaced by jellium which consists of delocalized electrons (electron gas), formed by the free electrons of the metal. The metal ions are imagined to be replaced by a constant positive background density. The energy required to embed an atom into this electron system is taken into account.

In EAM, the potential energy of atom i is determined by expression

$$E_i = F_i\left(\sum \rho_j(\boldsymbol{r}_{ij})\right) + \frac{1}{2}\sum V_{ij}(\boldsymbol{r}_{ij}) \tag{21}$$

where F_i is the energy required to embed an atom into the electron sea, ρ_j is the contribution to the electron density from atom j, r_{ij} is the distance between atoms i and j and V_{ij} is a pair potential interaction. The functions ρ and V are material dependent and determined by e.g. fitting the potential to experimental or ab-initio results. Because the range of such interactions is limited, and because the number of particles can be very high in atomistic simulations, only the contributions of the nearest neighbors or also the next-nearest neighbors j are usually included in the energy calculation by utilizing the concept of a cut-off distance.

This EAM potential gives a good description of a range of various Au properties crucial for simulations of collision cascades and sputtering processes, such as the surface energy and the melting temperature [108]. It has also demonstrated a good agreement with experimental results in the simulation of surface irradiation effects [99, 109–111], which is important for realistic modeling of high energy Xe ions impacts on Au nanorods. To simulate high-energy collisions in cascades produced after Xe ions impacts the universal Ziegler–Biersack–Littmark (ZBL) repulsive potential was used at small interatomic distances to complement the EAM potential. ZBL electronic stopping power was applied for all atoms with a kinetic energy ≥ 5 eV [112].

Xe ions were fired from random sites above the surface of the nanorod; the angles between the nanorod axis and the ion trajectories were selected randomly in the range $90° \pm 20°$.

The upper plane of the nanorod represented a (100) Au surface. We have estimated that the maximal temperature of the nanorod after each impact cannot exceed 800 K when irradiated by 80 keV Xe ions. Using the black body radiation law, we calculated that radiative cooling of the nanowire is very small and can be neglected in this case. After each irradiation, the system was relaxed for 200 ps without any temperature control. All sputtered atoms and clusters were then removed and the nanowire was cooled down to 300 K to mimic the experimental situation of a thermal conductive cooling through the Formvar film.

5.3 Results

The final shape of the nanorod following 32 ion impacts is presented in Fig. 19a. Deeper located atomic layers are colored in lighter tones to enhance the visibility of craters formed after the ion impacts. Although similar craters have been observed for some impact events in the real experiment [Publication **I**], they generally disappear during subsequent impacts. This can be explained by ion-induced localized flow events, coupled with surface tension effects [101], resulting in a smoothing of the surface roughness when impact points are close to the previous ones. As the number of impacts simulated by MD was about an order of magnitude smaller than those occurring during the experiment, this may partially explain the greater number of individual craters observed in the MD simulations.

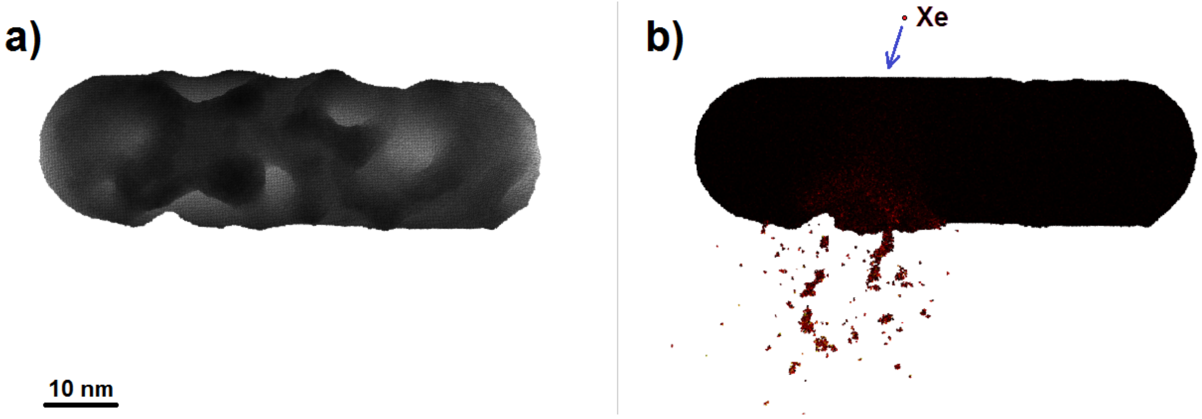

Figure 19: Results of MD simulation of 80 keV Xe^+ ions impacts on the Au nanorod: (a) Final shape of the nanorod after 32 consecutive ion impacts; lighter color represents deeper atomic layers (b) Snapshot at 25 ps following a single ion impact showing a formed crater and ejected nanoclusters. Clusters containing two atoms, and individual sputtered atoms are not shown for better visibility. From Publication III.

Fig. 19b illustrates cluster emission, an important process which is generally not taken into account in the standard models of sputtering, but appears to be at least partially responsible for the enhanced yields. Clusters are ejected as a result of thermal spike events intersecting with the surface and appear to provide the major component of the

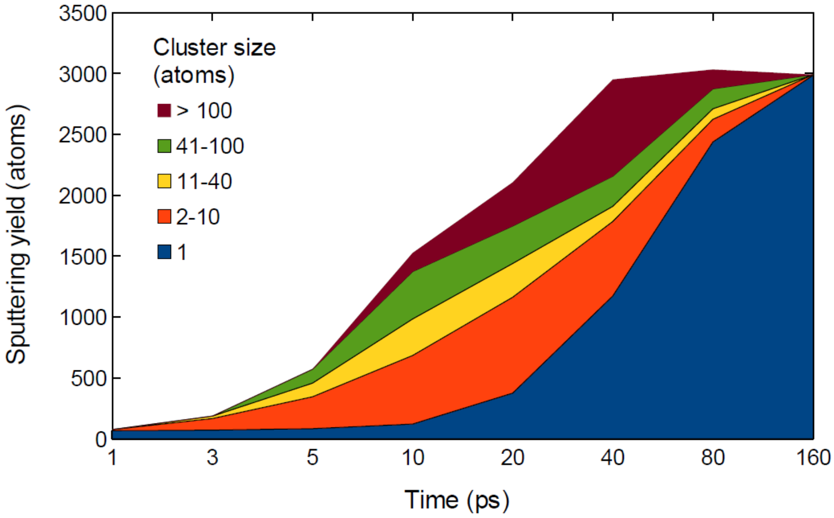

Figure 20: Cumulative diagram showing a contribution of Au nanoclusters of different size to the total yield over time for the single 80 keV Xe$^+$ ion impact presented on Fig. 19(b). The predominance of individual sputtered atoms at 80–100 ps is because all of the nanoclusters have disintegrated by the end of the simulation for this particular event (for some other events the biggest clusters stayed intact). From Publication III.

huge yields. This can be seen in Fig. 20, where the contribution of nanoclusters of different sizes to the total sputtering yield for the single event is presented. At 10 ps more than 90% of the total amount of ejected Au was in the form of clusters. The biggest clusters were mainly ejected during the latest stages of the spike event: from 20 to 40 ps. By the end of the simulation, however, the ejected atoms are observed entirely in the form of individual atoms, as all of the clusters have evaporated. Note that we have not implemented a radiative cooling model; it was not necessary for the nanowire itself due to the assumption of the conductive cooling through the Formvar film. However, this may be important for ejected nanoclusters having high temperature and big surface to volume ratios. Nevertheless, after several irradiation events, the biggest clusters were found to be intact even at the end of the simulations. These observations are qualitatively similar to those in [111], where it has also been reported that the majority of sputtered clusters dissipate. Clusters containing more than 100 atoms were observed in more than half of the 30 collisions we had simulated, where the ion was not incident along a channeling direction.

The ejection rate as a function of time for the event demonstrated on Fig. 19b, along with a corresponding cumulative sputtering yield is presented in Fig. 21. This graph clearly shows that the main contribution to the total yield was given by the material emitted as a result of the thermal spike process after 5 ps. The sputtering happens due to a localized melting and 'explosive' ejection of the molten material when the spike intersects with the surface. The contribution of the 'ordinary' ballistic and evaporative processes is ≈ 100 out of a total S of 2560 for this event. After 60 ps, a negative ejection rate is observed, and the total number of sputtered Au atoms decreases by ≈ 500 due to the redeposition effect: when hot sputtered clusters break up by evaporation, the atoms go in

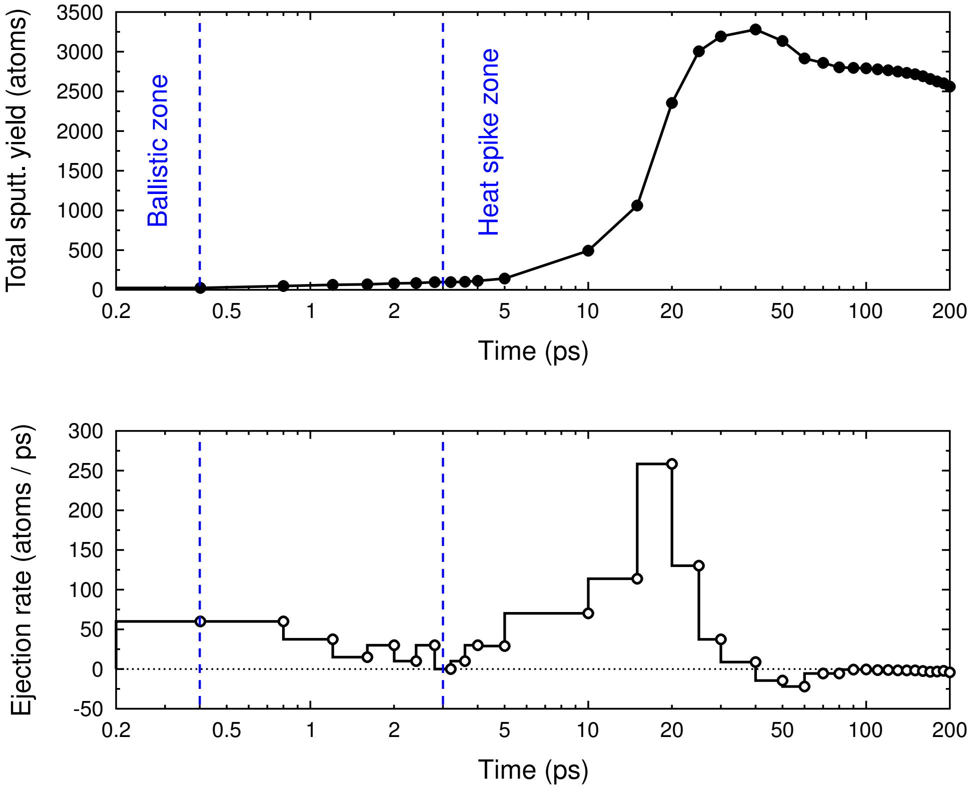

Figure 21: Cumulative sputtering yield and ejection rate as functions of time for the single 80 keV Xe$^+$ ion impact presented in Fig. 19(b). Each step on the ejection rate plot represents the mean ejection rate for the period since the previous time interval. Ballistic and evaporative processes are expected to be responsible for the sputtering up to 3 ps. The decrease of the total yield from 60 ps is due to the redeposition processes.

random directions, and some may redeposit back on the nanorod [111]. The average yield from 32 simulated impacts was 980 ± 180, with the maximal value for a single ion impact of 3159 sputtered atoms. When the incident Xe ion was aligned with the channeling direction the yield typically decreased to 0, because of the very small amount of energy transmitted from the ion to the nanowire when channeling occurs.

It is known that sputtering yields can be enhanced by off-normal incidence [105, 106], and irradiation of a cylindrical nanowire obviously involves all possible angles with respect to the surface normal. To investigate the influence of the angle of incidence, we have simulated sputtering from a flat Au surface for seven different angles in the range between 0° and 85° off-normal; 20 impacts at different points of a bulk Au sample have been performed at each angle for statistics. The results are presented in Fig. 22. Using a geometrical model of the nanorod (cylinder with hemispherical caps) we numerically estimated the distribution of impacts over the different angles of incidence. Combining this with the data from Fig. 22 let us to estimate the expected sputtering yield due to the effects of the varied angles of incidence. This gives a significantly increased value of $S = 388 \pm 89$, which is much more than $S \approx 50$ from a flat Au surface under the normal incidence [105], but still less than the average yields from nanorods obtained in the MD simulations (≈ 1000). This shows that the enhanced sputtering can only partly

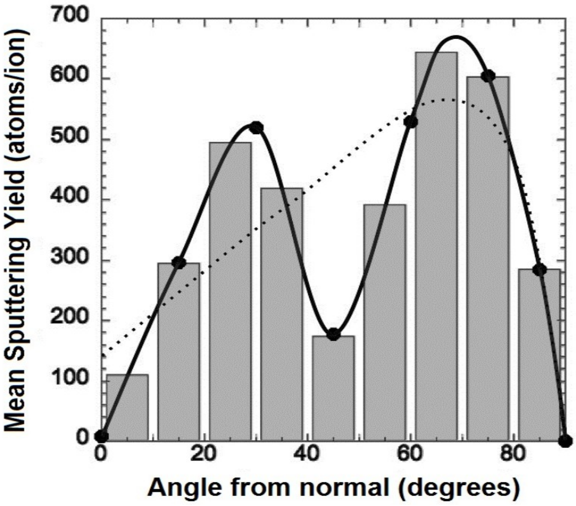

Figure 22: Angular dependence of the sputtering yields for a flat Au (100) surface under 80 keV Xe$^+$ ion irradiation, simulated by MD. The low values observed at 0° and 45° are due to channeling. The solid line is a polynomial fit to the data. The dotted line is an expected shape of the angular dependence if the orientation of the crystalline Au structure such that the alignment with channels is avoided; i.e. the average yields over all angles should be approximately the same if the distribution of random angles is uniform [113]. From Publication III.

be attributed to off-normal incidence angles at the nanowire, which means that nanosize effects make an important contribution to the yield enhancement.

To estimate the possibility of channeling and its influence on sputtering yields, the range calculations of 80 keV Xe ions on Au single crystals of different orientations have been performed using the MDRANGE code [112], which employs MD calculations, but forces are calculated only for those atoms that are involved in collision cascades for better computational efficiency; this method has previously demonstrated a good description of ion ranges in crystal channels in GaN and GaAs samples of different orientation [55, 114]. Au atoms were arranged in perfect crystal lattice sites; they were then randomly displaced from the equilibrium positions according to the Debye model, with a Debye temperature of 170 K that represents thermal displacements at 300 K. [115]. The tested surface normals were in the <100>, <110>, <111>, or <112> crystal direction and the twist ϕ angle of the incident ion was selected randomly [Publication **III**]. The calculated half-angle of channeling for 80 keV Xe ions on Au was from 3° to 5° for the four directions; similarly wide channels have also been observed in experiments [117]. Mean ranges were enhanced by factors of 4-10 and, specifically in the <112> direction, the mean range was 53 ± 3 nm compared with the average 12.2 ± 0.2 nm in non-channeling directions. With a mean range more than twice longer than the nanorod diameter, this results only in a small fraction of energy deposited by channeled ions during their path through the nanorod. Given the wide half-angle for channeling and the possibility of both axial and planar channeling, this effect reasonably explains the wide range of values for S observed in the experiments.

In order to check whether the cluster emission is specific only for the nanorod geometry or whether it can also be observed during the irradiation of flat Au surfaces, we analyzed the size of the largest sputtered clusters. We found that the average size of the biggest cluster sputtered from the nanorod was around 400 atoms in our simulations, whereas for the bulk cases it was ≈ 200 or less for all incoming angles. The number of clusters emitted in the nanorod irradiations was also greater on average. For instance, the mean number of clusters bigger than 100 atoms in size emitted from the nanorod at 40 ps snapshots was 0.82, while for the flat Au surface it was just 0.27. The larger surface area and surface curvature of a nanorod gives rise to the emission of a significantly larger number of atoms in clusters than in the case of ion irradiation of a flat surface.

A combination of different factors including surface proximity, varied angles of incidence and the explosive emission of atomic clusters due to the thermal spikes is responsible for a significant enhancement of sputtering yields for Xe ion impacts on Au nanorods, over those from flat Au surfaces. Although simulations reveal that clusters can also be emitted in the latter case, they are in average smaller and emitted more seldom. Such factors should also apply, to varying degrees, for heavy-ion collisions on other types of nanostructure made of dense materials. This needs to be taken into account when using ion beams processing on dense materials.

6 Discussion and Conclusions

In the first part of the thesis we studied mechanical properties of Si nanorods by MD simulations. The tested nanorods had sizes 5.8×31 nm, 7.9×46 nm, 10.4×62 nm, and 5.8×63 nm in the pristine state (as expected, the diameter grew during the imitated oxidation). Our simulations have revealed that there was no significant influence of a nanorod diameter on the Young's modulus obtained during a simple tensile test. The values for the pristine and completely oxidized nanorods were the same as for the simulated bulk Si and silica samples within the error bars. In comparison with the Young's moduli values from the real experiments [81], the MD values are underestimated for both Si and silica, when the Tersoff-Munetoh Si-O potential [31] is used. However, our tests have indicated, that the aforementioned potential represents the elastic properties of various Si-O compounds more realistically than the Samela-Watanabe potential [74].

We found that the addition of the oxide layer reduced the nanorods stiffness, in spite of the fact that the oxidized nanorods had larger diameters due to the additional oxygen atoms. The simple core shell model [21] which takes into account the cross-sectional area occupied by a crystalline Si core and an amorphous silica shell, described perfectly the Young's moduli of the partially oxidized nanorods. So, from the simple tensile tests no size related effects on the elastic behavior of nanorods have been observed.

Real Si nanowires with diameters of such orders of magnitude have not been tested thoroughly yet as they are very difficult to produce and manipulate. For example, Sohn et. al [27] has investigated the elastic properties of Si nanowires with diameters in range from 100 nm to 600 nm and concluded that at such dimensions the finite size effects do not play any role on the elastic behavior.

To simulate bending behavior during a three point flexural nanoscale test - a very common technique used in real experiments for nanowires characterization, similar boundary conditions have been implemented in the atomistic model. After that, we used the stress tensor values obtained from the MD simulations as an input for the FEM model for nanorods of the same characteristic sizes. FEM model was needed to check the validity of the classical continuum mechanics approximations - as it lets us to simulate easily bending of nanowires having the specific geometry, small length-to-diameter ratio, taking into account anisotropy of the crystalline core and intrinsic stresses.

Our simulations have revealed that the effective bending moduli of the nanorods calculated by MD were bigger (stiffer), than predicted by FEM when the elasticity constants obtained from MD bulk simulations were used in the FEM model. This was not, however, true for two of the smallest completely oxidized silica nanorods. As they had the same Young's moduli as the other silica nanorods (demonstrated in the earlier tensile simulations), we concluded that such difference should be attributed to the drop of the shear modulus, due to effects of the microstructure of amorphous silica nanorods. Similar decrease of the shear modulus has been predicted in [96], where the author analyzed analytically the influence of size effects on the shear modulus of amorphous and crystalline nanorods; their conclusion was that such decrease is especially notable for the amorphous materials.

Addition of the intrinsic surface stresses to the FEM model did not affect much the bending properties; however, the stresses in the oxide shell had a much bigger influence on the bending modulus. It is important to realize, that the oxide layer has been added artificially in this work, but not by the realistic oxidation process, so the stress values may not be entirely correct for the partially oxidized Si nanorods. To our knowledge, stress tensors for nanowires have not been measured in real experiments yet, nor the results of the ReaxFF oxidation simulations can be trusted, as MD does not let to simulate oxidation in normal ambient conditions and relax stresses in the oxide layer for long enough time. Therefore, it is difficult to verify the validity of the obtained stress tensor values.

More analysis may be needed to understand the reasons of stiffening (in comparison with FEM) during the bending tests, observed in our MD simulations. The FEM model could be improved by including the effect of modification of elastic properties near the surface layer. It has been demonstrated by the recent ab-initio calculations [97, 118, 119], that electronic structure effects at surfaces play an important role in the elastic behavior of nanowires. Zhou et al. showed [97] that there are two competing phenomena, which determine the overall behavior: stiffening because of the bond saturation resulting from the local electronic redistribution on the surfaces (higher electron density on the surface - stronger bonding); and softening induced by coordination number reduction due to missing neighbors. Lee et al. has observed [119] softening effect for Si nanowires with diameters smaller than 4 nm from ab-initio calculations; this effect disappeared for bigger diameters. They also found, that nonlinear bulk elasticity has a negligible effect on the Young's modulus of the tested nanowires.

The classical MD potentials are sufficiently good for simulating nanosystems of realistic sizes, but, as they have been fitted mostly to the bulk material properties and the electronic effects involved in surface reconstructions are not taken into account in pure MD calculations, their predictive capabilities are expected to be limited for estimating the elastic properties of surfaces at the nanoscale. There is a significant need for efficient methods based on ab-initio calculations, which can simulate big enough structures taking into account the surface effects.

In the second part of the thesis, we investigated sputtering from Au nanorods under 80 keV Xe ion bombardment. Large yields, similar to those as from the real experiment (≈ 1000 atoms per impact) have been observed in our MD simulations; the characteristic sizes and the structure of the nanorods were the same sizes as in the experimental setup.

To understand the reason of such big yields, we have firstly estimated the enhancement that is attributed to the various incidence angles between the incoming ion and the cylindrical nanowire. The simulations of sputtering yields from the flat Au surface had been done for different incident angles, and the random angles distribution was estimated according to the geometrical parameters of the nanorod. We have found, that these factors can enhance the expected sputtering up to 400 atoms per ion. It means, that the effect of the various incident angles is important, but still alone cannot explain the observed sputtering yields.

We had done the analysis of the sputtered atoms and found, that ejected clusters are observed in all events which resulted in yields more than 500 atoms. Though the cluster sputtering has also been observed from the flat Au surface, the clusters ejected from the nanorods are in average larger, and their number is bigger. This can be attributed to the effect of a large surface area and the cylindrical shape of the nanorod, so it is more probable that a thermal spike intersects with the surface, and a big amount of the molten material is ejected from the curved surface in a form of clusters.

Our range simulations have confirmed large half-angles of channeling for certain crystal directions, which can explain big variations of the average sputtering yields from different nanorods, observed both in the experiment and in our MD simulations. If the incoming beam happens to be aligned with a crystal axis of the nanorod, the very small amount of energy is deposited and a yield can decrease to less than 100 atoms per impact.

The observed large sputtering yields were mainly caused by the combination of the material of the nanowires - gold, which is dense but has a low melting temperature (increases the probability of a thermal spike), and the ion energies resulted in ranges comparable with the diameter of the nanorods (increases the probability of a thermal spike to intersect with the surface). This should be taken into account when the radiation processing of similar nanostructures is performed.

ACKNOWLEDGEMENTS

I wish to thank the former head of the Department of Physics at the University of Helsinki, Prof. Juhani Keinonen, and the current head, Prof. Hannu Koskinen, as well as the head of the Accelerator Laboratory, Prof. Jyrki Räisänen, for providing the facilities for the research presented in this thesis. Financial support from the Academy of Finland and the travel grants provided by the National Doctoral Programme in Nanoscience are gratefully acknowledged.

I thank Prof. Roman Nowak and Dr. Timo Sajavaara for the pre-examination of my thesis and their many wise and rational comments. I am also thankful to Prof. Stefan Mayr for agreeing to be my opponent in the public examination of this thesis.

I am deeply grateful to my supervisor Dr. Antti Kuronen and my co-supervisor Prof. Kai Nordlund for their guidance, encouragement, support, inspirational ideas and scientific expertise shared during working hours, while at the same time being nice, helpful and interesting persons in everyday life. I would also like to show my gratitude to Doc. Flyura Djurabekova; she has not been my direct supervisor but helped numerous times with her advice and also made the coffee breaks and lunches lively with her stories. Thank you! I would also like to thank Prof. Stephen Donnelly from University of Huddersfield for his advice and assistance during our collaboration and, of course, for his ultimate English proficiency; it is very nice to prepare a manuscript knowing that there is a person who can help to express the ideas in a perfect language.

I would also like to thank people related to the operation and support of the Accelerator Laboratory IT infrastructure: Pekko Metsä, Sisko Vikberg, Eero, Stefan and Morten. It was a very interesting and useful experience being a part of you. Thank you for the professional help, smart suggestions, and, of course, for the fact that everything is running perfectly.

During my work on this thesis my office mates have always been of a great support. Thank you Jussi, Laura and Wei for providing such a pleasant and interesting work environment. I also wish to extend my thanks to all my other friends from Accelerator Laboratory and outside, for creating a warm and welcoming atmosphere, for your support and useful advice!

And, most of all, I want to thank my parents and relatives, my wife Natalia and our daughter Victoria for their love and support at home, who made all this possible and meaningful.

Helsinki, February 5th, 2015

Andrey

References

[1] G. Binnig, H. Rohrer, C. Gerber, and E. Weibel, "Surface studies by scanning tunneling microscopy," *Phys. Rev. Lett.*, vol. 49, pp. 57–61, Jul 1982.

[2] P. Ricciardi, P. Colomban, A. Tournie, M. Macchiarola, and N. Ayed, "A non-invasive study of roman age mosaic glass tesserae by means of raman spectroscopy," *Journal of Archaeological Science*, vol. 36, no. 11, pp. 2551 – 2559, 2009.

[3] Wikipedia, "Applications of nanotechnology," 2014, [Online; Accessed 19.09.2014].

[4] I. Sondi and B. Salopek-Sondi, "Silver nanoparticles as antimicrobial agent: a case study on e.coli as a model for gram-negative bacteria," *Journal of Colloid and Interface Science*, vol. 275, no. 1, pp. 177 – 182, 2004.

[5] T. G. Smijs and S. Pavel, "Titanium dioxide and zinc oxide nanoparticles in sunscreens: focus on their safety and effectiveness." *Nanotechnol. Sci. Appl.*, vol. 4, pp. 95–112, Jan. 2011.

[6] J. Chen, B. J. Wiley, and Y. Xia, "One-dimensional nanostructures of metals: large-scale synthesis and some potential applications," *Langmuir*, vol. 23, no. 8, pp. 4120–4129, 2007.

[7] R. Agrawal and H. D. Espinosa, "Multiscale Experiments: State of the Art and Remaining Challenges," *J. Eng. Mater. Technol.*, vol. 131, no. 4, p. 041208, 2009.

[8] A. T. Gordon, G. E. Lutz, M. L. Boninger, and R. A. Cooper, "Introduction to nanotechnology: potential applications in physical medicine and rehabilitation," *American journal of physical medicine and rehabilitation*, vol. 86, no. 3, pp. 225–241, 2007.

[9] Q. Li, S. Mahendra, D. Y. Lyon, L. Brunet, M. V. Liga, D. Li, and P. J. Alvarez, "Antimicrobial nanomaterials for water disinfection and microbial control: potential applications and implications," *Water research*, vol. 42, no. 18, pp. 4591–4602, 2008.

[10] M. J. Bierman and S. Jin, "Potential applications of hierarchical branching nanowires in solar energy conversion," *Energy and Environmental Science*, vol. 2, no. 10, pp. 1050–1059, 2009.

[11] N. Sozer and J. L. Kokini, "Nanotechnology and its applications in the food sector," *Trends in biotechnology*, vol. 27, no. 2, pp. 82–89, 2009.

[12] J. Wilkinson, "Nanotechnology applications in medicine." *Medical device technology*, vol. 14, no. 5, pp. 29–31, 2003.

[13] J. Sarkar, G. G. Khan, and A. Basumallick, "Nanowires : properties , applications and synthesis via porous anodic aluminium oxide template," *Bull. Mater. Sci*, vol. 30, no. 3, pp. 271–290, 2007.

[14] D. Chrobak, N. Tymiak, A. Beaber, O. Ugurlu, W. W. Gerberich, and R. Nowak, “Deconfinement leads to changes in the nanoscale plasticity of silicon.” *Nat. Nanotechnol.*, vol. 6, no. 8, pp. 480–4, Aug. 2011.

[15] V. N. Tuoc, “The self-consistent charge density functional tight binding study on wurtzite nanowire,” *Comput. Mater. Sci.*, vol. 49, no. 4, pp. S161–S169, Oct. 2010.

[16] D. A. Smith, V. C. Holmberg, D. C. Lee, and B. A. Korgel, “Young’s Modulus and Size-Dependent Mechanical Quality Factor of Nanoelectromechanical Germanium Nanowire Resonators,” *J. Phys. Chem. C*, vol. 112, no. 29, pp. 10 725–10 729, Jul. 2008.

[17] E. Ivanova, A. Krivtsov, and N. Morozov, “Bending stiffness calculation for nanosize structures,” *Fatigue Fract. Eng. Mater. Struct.*, vol. 26, no. August 2002, pp. 715–718, 2003.

[18] J. Gere and B. Goodno, *Mechanics of Materials.* Cengage Learning, 2009.

[19] C. Chen, Y. Shi, Y. Zhang, J. Zhu, and Y. Yan, “Size Dependence of Young’s Modulus in ZnO Nanowires,” *Phys. Rev. Lett.*, vol. 96, no. 7, pp. 1–4, Feb. 2006.

[20] X. Li, W. Hu, S. Xiao, and W.-Q. Huang, “Molecular dynamics simulation of polycrystalline molybdenum nanowires under uniaxial tensile strain: Size effects,” *Physica E*, vol. 40, no. 10, pp. 3030–3036, Sep. 2008.

[21] F. Xu, Q. Qin, A. Mishra, Y. Gu, and Y. Zhu, “Mechanical properties of ZnO nanowires under different loading modes,” *Nano Res.*, vol. 3, no. 4, pp. 271–280, Mar. 2010.

[22] Y. Tong, F. J. Yi, L. S. Liu, and Q. J. Zhang, “Molecular Dynamics Simulation of Mechanical Properties of Single-Crystal Bismuth Telluride Nanowire,” *J. Electron. Mater.*, vol. 39, no. 9, pp. 1730–1734, Apr. 2010.

[23] R. He and P. Yang, “Giant piezoresistance effect in silicon nanowires.” *Nat. Nanotechnol.*, vol. 1, no. October, pp. 42–46, 2006.

[24] M. Messina and J. Njuguna, “Potential of silicon nanowires structures as nanoscale piezoresistors in mechanical sensors,” *IOP Conf. Ser. Mater. Sci. Eng.*, vol. 40, p. 012038, 2012.

[25] Z. L. Wang, “ZnO nanowire and nanobelt platform for nanotechnology,” *Mater. Sci. Eng. R Reports*, vol. 64, no. 3-4, pp. 33–71, Apr. 2009.

[26] A. Furmanchuk, O. Isayev, T. C. Dinadayalane, D. Leszczynska, and J. Leszczynski, “Mechanical properties of silicon nanowires,” *WIRES Comp. Mol. Sci.*, vol. 2, no. 6, pp. 817–828, 2012.

[27] Y.-S. Sohn, J. Park, G. Yoon, J. Song, S.-W. Jee, J.-H. Lee, S. Na, T. Kwon, and K. Eom, “Mechanical Properties of Silicon Nanowires.” *Nanoscale Res. Lett.*, vol. 5, no. 1, pp. 211–216, Jan. 2009.

[28] D.-M. Tang, C.-L. Ren, M.-S. Wang, X. Wei, N. Kawamoto, C. Liu, Y. Bando, M. Mitome, N. Fukata, and D. Golberg, “Mechanical properties of Si nanowires as revealed by in situ transmission electron microscopy and molecular dynamics simulations.” *Nano Lett.*, vol. 12, no. 4, pp. 1898–904, Apr. 2012.

[29] S.-H. Shin, G.-Y. Kim, J. Shim, J. Kim, H.-G. Hur, D.-J. Lee, J.-I. Song, and S.-H. Moon, “Use of biologically designed gold nanowire for biosensor application,” *Korean Journal of Chemical Engineering*, vol. 29, no. 12, pp. 1666–1669, 2012.

[30] G. Greaves, J. A. Hinks, P. Busby, N. J. Mellors, A. Ilinov, A. Kuronen, K. Nordlund, and S. E. Donnelly, “Enhanced Sputtering Yields from Single-Ion Impacts on Gold Nanorods,” *Phys. Rev. Lett.*, vol. 111, no. 6, p. 065504, Aug. 2013.

[31] S. Munetoh, T. Motooka, K. Moriguchi, and A. Shintani, “Interatomic potential for Si–O systems using Tersoff parameterization,” *Comput. Mater. Sci.*, vol. 39, no. 2, pp. 334–339, Apr. 2007.

[32] B. J. Alder and T. E. Wainwright, “Molecular dynamics by electronic computers,” ser. Proc. Intern. Symposium on Transport Processes in Statistical Mechanics. New York: Wiley Interscience, 1957, p. 97.

[33] B. J. Alder and T. E. Wainwright, “Studies in molecular dynamics. i. general method,” *J. of Chem. Phys.*, vol. 31, no. 2, p. 459, 1959.

[34] V. Springel, “The cosmological simulation code gadget-2,” *Monthly notices of the royal astronomical society*, vol. 364, no. 4, p. 1105, 2005.

[35] L. Verlet, “Computer “experiments” on classical fluids. i. thermodynamical properties of lennard-jones molecules,” *Phys. Rev.*, vol. 159, p. 98, 1967.

[36] C. W. Gear, *Numerical initial value problems in ordinary differential equations.* Englewook Cliffs, NJ, USA: Prentice-Hall, 1971.

[37] H. J. C. Berendsen, J. P. M. Postma, W. F. van Gunsteren, A. DiNola, and J. R. Haak, “Molecular dynamics with coupling to external bath,” *J. Chem. Phys.*, vol. 81, no. 8, p. 3684, 1984.

[38] S. Nosé, “A unified formulation of the constant temperature molecular dynamics methods,” *J. Chem. Phys.*, vol. 81, no. 1, p. 511, 1984.

[39] H. Andersen, “Molecular-dynamics simulations at constant pressure and-or temperature,” *J. Chem. Phys.*, vol. 72, no. 4, p. 2384, 1980.

[40] B. L. Holian, A. F. Voter, and R. Ravelo, “Thermostatted molecular dynamics: How to avoid the toda demon hidden in nose-hoover dynamics,” *Phys. Rev. E*, vol. 52, pp. 2338–2347, 1995.

[41] M. P. Allen and D. J. Tildesley, *Computer Simulation of Liquids.* Oxford, England: Oxford University Press, 1989.

[42] K. Nordlund, M. Ghaly, R. S. Averback, M. Caturla, T. D. de la Rubia, and J. Tarus, “Defect production in collision cascades in elemental semiconductors and fcc metals,” *Phys. Rev. B*, vol. 57, p. 7556, 1998.

[43] M. Ghaly, K. Nordlund, and R. S. Averback, *Phil. Mag. A*, vol. 79, p. 795, 1995.

[44] H. H. Andersen and J. F. Ziegler. New York: Pergamon, 1977, vol. 3.

[45] J. F. Ziegler, J. P. Biersack, and U. Littmark, *The Stopping and Range of Ions in Matter.* New York: Pergamon, 1985.

[46] J. F. Ziegler, SRIM-2013 software package, available online at *http://www.srim.org.*

[47] R. Smith (ed.), *Atomic & ion collisions in solids and at surfaces: theory, simulation and applications.* Cambridge, UK: Cambridge University Prss, 1997.

[48] Wikipedia, “Electronic nuclear stopping al in al,” 2014, [Online; Accessed 30.11.2014].

[49] T. Diaz de la Rubia, R. S. Averback, R. Benedek, and W. E. King, “Role of thermal spikes in energetic collision cascades,” *Phys. Rev. Lett.*, vol. 59, pp. 1930–1933, 1987, see also erratum: Phys. Rev. Lett. 60 (1988) 76.

[50] A. E. Stuchbery and E. Bezakova, “Thermal-spike lifetime from picosecond-duration preequilibrium effects in hyperfine magnetic fields following ion implantation,” *Phys. Rev. Lett.*, vol. 82, no. 18, p. 3637, 1999.

[51] W. M. Young and E. W. Elcock, “Monte carlo studies of vacancy migration in binary ordered alloys: I,” *Proc. Phys. Soc*, vol. 89, pp. 735–746, 1966.

[52] A. E. Sand, S. L. Dudarev, and K. Nordlund, “High energy collision cascades in tungsten: dislocation loops structure and clustering scaling laws,” *EPL*, vol. 103, p. 46003, 2013.

[53] A. Caro and M. Victoria, “Ion-electron interaction in molecular-dynamics cascades,” *Phys. Rev. A (General Physics)*, vol. 40, no. 5, pp. 2287–91, 1989.

[54] J. le Page, D. R. Mason, C. P. Race, and W. M. C. Foulkes, “How good is damped molecular dynamics as a method to simulate radiation damage in metals?” *New J. Phys.*, vol. 11, p. 013004, 2009.

[55] J. Sillanpää, K. Nordlund, and J. Keinonen, “Electronic stopping of silicon from a 3d charge distribution,” *Phys. Rev. B*, vol. 62, p. 3109, 2000.

[56] J. F. Ziegler, J. P. Biersack, and M. D. Ziegler, *SRIM - The Stopping and Range of Ions in Matter.* Chester, Maryland, USA: SRIM Co., 2008.

[57] A. B. Migdal, “Bremsstrahlung and pair production in condensed media at high energies,” *Physical Review*, vol. 103, pp. 1811–1820, 1956.

[58] J. M. Pruneda and E. Artacho, “Short-range repulsive interatomic interactions in energetic processes in solids,” *Phys. Rev. B*, vol. 70, p. 035106, Jul 2004.

[59] K. Nordlund, N. Runeberg, and D. Sundholm, “Repulsive interatomic potentials calculated using hartree-fock and density-functional theory methods,” *Nucl. Instr. Meth. Phys. Res. B*, vol. 132, pp. 45–54, 1997.

[60] K. Nordlund, “Molecular dynamics simulation of atomic collisions for ion irradiation experiments,” *Acta Polytechnica Scandinavica, Applied Physics Series*, vol. 202, p. 1, 1995, PhD thesis, University of Helsinki.

[61] H. S. Park, W. Cai, H. D. Espinosa, and H. Huang, “Mechanics of Crystalline Nanowires,” *MRS Bull.*, vol. 34, no. 2009, pp. 178–183, 2009.

[62] P. Zhou, C. Wu, and X. Li, “Three-point bending Young’s modulus of nanowires,” *Meas. Sci. Technol.*, vol. 19, no. 11, p. 115703, Nov. 2008.

[63] H. Ni and X. Li, “Young’s modulus of ZnO nanobelts measured using atomic force microscopy and nanoindentation techniques.” *Nanotechnology*, vol. 17, no. 14, pp. 3591–7, Jul. 2006.

[64] M.-F. Yu, O. Lourie, M. J. Dyer, K. Moloni, T. F. Kelly, and R. S. Ruoff, “Strength and breaking mechanism of multiwalled carbon nanotubes under tensile load,” *Science*, vol. 287, no. 5453, pp. 637–640, 2000.

[65] R. E. Miller and V. B. Shenoy, “Size-dependent elastic properties of nanosized structural elements,” *Nanotechnology*, vol. 11, pp. 139–147, 2000.

[66] G. Jing, H. Duan, X. Sun, Z. Zhang, J. Xu, Y. Li, J. Wang, and D. Yu, “Surface effects on elastic properties of silver nanowires: Contact atomic-force microscopy,” *Phys. Rev. B*, vol. 73, no. 23, p. 235409, Jun. 2006.

[67] C. S. Zha, R. J. Hemley, H. K. Mao, T. S. Duffy, and C. Meade, “Acoustic velocities and refractive index of SiO2 glass to 57.5 GPa by Brillouin scattering,” *Phys. Rev. B*, vol. 50, no. 18, pp. 13 105–13 112, 1994.

[68] S. Billeter, A. Curioni, D. Fischer, and W. Andreoni, “Ab initio derived augmented Tersoff potential for silicon oxynitride compounds and their interfaces with silicon,” *Phys. Rev. B*, vol. 73, no. 15, pp. 1–15, Apr. 2006.

[69] T. Watanabe, D. Yamasaki, K. Tatsumura, and I. Ohdomari, “Improved interatomic potential for stressed Si, O mixed systems,” *Appl. Surf. Sci.*, vol. 234, no. 1-4, pp. 207–213, Jul. 2004.

[70] S. Lee, R. Bondi, and G. Hwang, “Ab initio parameterized valence force field for the structure and energetics of amorphous SiOx materials,” *Phys. Rev. B*, vol. 84, no. 4, pp. 1–13, Jul. 2011.

[71] S. von Alfthan, A. Kuronen, and K. Kaski, “Realistic models of amorphous silica: a comparative study of different potentials,” *Phys. Rev. B*, vol. 68, p. 073203, Aug 2003.

[72] M. J. Buehler, A. C. T. Van Duin, and W. a. Goddard, “Multiparadigm modeling of dynamical crack propagation in silicon using a reactive force field,” *Phys. Rev. Lett.*, vol. 96, no. March, pp. 1–4, 2006.

[73] J. Samela, K. Nordlund, V. Popok, and E. Campbell, “Origin of complex impact craters on native oxide coated silicon surfaces,” *Phys. Rev. B*, vol. 77, no. 7, Feb. 2008.

[74] J. Samela, “Molecular dynamics studies of nanoparticle impacts,” Ph.D. dissertation, University of Helsinki, 2008.

[75] F. H. Stillinger and T. A. Weber, “Computer simulation of local order in condensed phases of silicon,” *Phys. Rev. B*, vol. 31, p. 5262, 1985.

[76] S. von Alfthan, A. Kuronen, and K. Kaski, “Realistic models of amorphous silica: A comparative study of different potentials,” *Phys. Rev. B*, vol. 68, p. 073203, 2003.

[77] M. Backman, F. Djurabekova, O. H. Pakarinen, K. Nordlund, L. L. Araujo, and M. C. Ridgway, “Amorphization of ge and si nanocrystals embedded in amorphous sio_2 by ion irradiation,” *Phys. Rev. B*, vol. 80, p. 144109, Oct 2009.

[78] F. Djurabekova and K. Nordlund, “Atomistic simulation of the interface structure of Si nanocrystals embedded in amorphous silica,” *Phys. Rev. B*, vol. 77, no. December 2007, pp. 1–7, 2008.

[79] F. Wooten, K. Winer, and D. Weaire, “Computer generation of structural models of amorphous si and ge,” *Phys. Rev. Lett.*, vol. 54, pp. 1392–1395, Apr 1985.

[80] W. Ren, A. Kuronen, and K. Nordlund, “Molecular dynamics of irradiation-induced defect production in GaN nanowires,” *Phys. Rev. B*, vol. 86, no. 10, pp. 1–7, Sep. 2012.

[81] O. Madelung, U. Rössler, and M. Schulz, Eds., *Silicon (Si) Young’s modulus, torsion modulus, bulk modulus (various structures)*, ser. Landolt-Börnstein - Group III Condensed Matter. Springer Berlin Heidelberg, 2001, vol. 41A1a, pp. 1–12.

[82] I. Ponomareva, M. Menon, D. Srivastava, and A. N. Andriotis, “Structure, Stability, and Quantum Conductivity of Small Diameter Silicon Nanowires,” *Phys. Rev. Lett.*, vol. 95, no. 26, pp. 1–4, Dec. 2005.

[83] R. Smith, D. Christopher, S. Kenny, A. Richter, and B. Wolf, “Defect generation and pileup of atoms during nanoindentation of Fe single crystals,” *Phys. Rev. B*, vol. 67, no. 24, p. 245405, Jun. 2003.

[84] U. Khalilov, G. Pourtois, a. C. T. V. Duin, and E. C. Neyts, “Self-limiting oxidation in small-diameter Si nanowires,” *Chem. Mater.*, vol. 24, pp. 2141–2147, 2012.

[85] U. Khalilov, E. C. Neyts, G. Pourtois, and A. C. T. van Duin, “Can We Control the Thickness of Ultrathin Silica Layers by Hyperthermal Silicon Oxidation at Room Temperature?” *J. Phys. Chem. C*, vol. 115, no. 50, pp. 24 839–24 848, Dec. 2011.

[86] U. Khalilov, G. Pourtois, A. C. T. van Duin, and E. C. Neyts, “On the c -Si| a -SiO 2 Interface in Hyperthermal Si Oxidation at Room Temperature,” *J. Phys. Chem. C*, vol. 116, no. 41, pp. 21 856–21 863, Oct. 2012.

[87] U. Khalilov, G. Pourtois, A. C. T. van Duin, and E. C. Neyts, “Hyperthermal oxidation of si(100)2x1 surfaces: Effect of growth temperature,” *J. Phys. Chem. C*, vol. 116, no. 15, pp. 8649 – 8656, apr 2012.

[88] M. Morita, T. Ohmi, E. Hasegawa, M. Kawakami, and M. Ohwada, “Growth of native oxide on a silicon surface,” *J. Appl. Phys.*, vol. 68, no. 3, p. 1272, 1990.

[89] M. X. Shi, B. Liu, Z. Q. Zhang, Y. W. Zhang, and H. J. Gao, “Direct influence of residual stress on the bending stiffness of cantilever beams,” *Proc. R. Soc. A Math. Phys. Eng. Sci.*, vol. 468, no. 2145, pp. 2595–2613, Mar. 2012.

[90] B.-H. Kim, M. Ariesto Pamungkas, M. Park, G. Kim, K.-R. Lee, and Y.-C. Chung, “Stress evolution during the oxidation of silicon nanowires in the sub-10 nm diameter regime,” *Applied Physics Letters*, vol. 99, no. 14, p. 143115, Oct. 2011.

[91] U. Khalilov, G. Pourtois, A. Bogaerts, A. C. T. van Duin, and E. C. Neyts, “Reactive molecular dynamics simulations on sio2-coated ultra-small si-nanowires,” *Nanoscale*, vol. 5, pp. 719–725, 2013.

[92] A. Ilinov and A. Kuronen, “Atomistic modeling of bending properties of oxidized silicon nanowires,” *J. Appl. Phys.*, vol. 115, no. 10, p. 104305, Mar. 2014.

[93] R. Roark, *Formulas for Stress and Strain.* McGraw-Hill, New York, 1965.

[94] O. Zienkiewicz and R. Taylor, *The Finite Element Method: Solid mechanics*, ser. Referex collection.Mecánica y materiales. Butterworth-Heinemann, 2000.

[95] COMSOL Multiphysics, COMSOL AB, 2014, http://www.comsol.com/.

[96] Y. Cohen and I. Procaccia, "Elastic moduli in nano-size samples of amorphous solids: System size dependence," *EPL (Europhysics Lett.*, vol. 99, no. 3, p. 46002, 2012.

[97] L. G. Zhou and H. Huang, "Are surfaces elastically softer or stiffer?" *Applied Physics Letters*, vol. 84, no. 11, 2004.

[98] M. T. McDowell, A. M. Leach, and K. Gall, "Bending and tensile deformation of metallic nanowires," *Modelling and Simulation in Materials Science and Engineering*, vol. 16, no. 4, p. 045003, 2008.

[99] M. Ghaly and R. S. Averback, "Effect of viscous flow on ion damage near solid surfaces," *Phys. Rev. Lett.*, vol. 72, no. 3, pp. 364–367, 1994.

[100] R. C. Birtcher and S. E. Donnelly, "Plastic flow produced by single ion impacts on metals," *Nucl. Instr. Meth. Phys. Res. B*, vol. 148, pp. 194–199, 1999.

[101] S. E. Donnelly and R. C. Birtcher, "Heavy ion cratering of gold," *Phys. Rev. B*, vol. 56, no. 21, p. 13599, 1997.

[102] H. H. Andersen, A. Brunelle, S. Della-Negra, J. Depauw, D. Jacquet, Y. Le Beyec, J. Chaumont, and H. Bernas, "Giant metal sputtering yields induced by 20-5000 kev/atom gold clusters," *Phys. Rev. Lett.*, vol. 80, p. 5433, 1998.

[103] K. Nordlund and F. Djurabekova, "Multiscale modelling of irradiation in nanostructures," *J. Comput. Electr.*, vol. 13, no. 1, p. 122, 2014, Invited review paper for special issue on device modelling.

[104] W. Qi and M. Wang, "Size and shape dependent melting temperature of metallic nanoparticles," *Materials Chemistry and Physics*, vol. 88, no. 2-3, pp. 280 – 284, 2004.

[105] R. Behrisch (ed.), *Sputtering by Particle bombardment I.* Berlin: Springer, 1981.

[106] J. M. Fluit, P. K. Roi, and J. Kistemaker, "Angular-dependent sputtering of copper single crystals," *J. Appl. Phys.*, vol. 34, p. 690, 1963.

[107] S. M. Foiles, M. I. Baskes, and M. S. Daw, "Embedded-atom-method functions for the fcc metals cu, ag, au, ni, pd, pt, and their alloys," *Phys. Rev. B*, vol. 33, no. 12, p. 7983, 1986, *Erratum: ibid,* Phys. Rev. B 37, 10378 (1988).

[108] M. S. Daw, S. M. Foiles, and M. I. Baskes, "The embedded-atom method: a review of theory and applications," *Mat. Sci. Rep.*, vol. 9, p. 251, 1993.

[109] K. Nordlund, J. Tarus, J. Keinonen, S. E. Donnelly, and R. C. Birtcher, "Atomic fingers, bridges and slingshots: formation of exotic surface structures during ion irradiation of heavy metals," *Nucl. Instr. Meth. Phys. Res. B*, vol. 206, pp. 189–193, 2003.

[110] J. Samela, J. Kotakoski, K. Nordlund, and J. Keinonen, "A quantitative and comparative study of sputtering yields in au," *Nucl. Instr. Meth. Phys. Res. B*, vol. 239, no. 4, pp. 331–346, 2005.

[111] K. O. E. Henriksson, K. Nordlund, and J. Keinonen, "Fragmentation of sputtered silver and gold clusters," *Phys. Rev. B*, vol. 71, p. 014117, 2005.

[112] K. Nordlund, "Molecular dynamics simulation of ion ranges in the 1 – 100 kev energy range," *Comput. Mater. Sci.*, vol. 3, p. 448, 1995.

[113] Y. Yamamura, Y. Itikawa, and N. Itoh, "Angular dependence of sputtering yields of monatomic solids," Institute of Plasma Physics, Nagoya University, Report IPPJ-AM-26, 1983.

[114] J. Peltola, K. Nordlund, and J. Keinonen, "Explicit phase shift factor stopping model for multi-component targets," *Nucl. Instr. Meth. Phys. Res. B*, vol. 212, p. 118, 2003.

[115] N. W. Ashcroft and N. D. Mermin, *Solid State Physics.* Philadelphia: Saunders College, 1976.

[116] A. Ilinov, A. Kuronen, K. Nordlund, G. Greaves, J. Hinks, P. Busby, N. Mellors, and S. Donnelly, "Sputtering yields exceeding 1000 by 80keV Xe irradiation of Au nanorods," *Nucl. Instruments Methods Phys. Res. Sect. B Beam Interact. with Mater. Atoms*, 2014.

[117] J. Nord, K. Nordlund, B. Pipeleers, and A. Vantomme, "Implantation angle dependence of ion irradiation damage in gan," *Materials Science and Engineering B*, vol. 105, no. 1, pp. 110–112, 2003.

[118] L. Zhang and H. Huang, "Young's moduli of zno nanoplates: Ab initio determinations," *Applied Physics Letters*, vol. 89, no. 18, pp. –, 2006.

[119] B. Lee and R. E. Rudd, "First-principles calculation of mechanical properties of Si001 nanowires and comparison to nanomechanical theory," *Phys. Rev. B - Condens. Matter Mater. Phys.*, vol. 75, pp. 1–13, 2007.